Allosteric modulation of the catalytic VYD loop in Slingshot by its N-terminal domain underlies both Slingshot auto-inhibition and activation

Received for publication, May 25, 2018, and in revised form, August 21, 2018 Published, Papers in Press, August 28, 2018, DOI 10.1074/jbc.RA118.004175

Duxiao Yang[‡1], Peng Xiao[‡§1], Qing Li[¶1], Xiaolei Fu[‡], Chang Pan[‡], Di Lu[‡], Shishuai Wen[§], Wanying Xia[‡], Dongfang He[‡], Hui Li[¶], Hao Fang[§], Yuemao Shen[§], Zhigang Xu[‖], Amy Lin[**], Chuan Wang[§§], Xiao Yu[¶], Jiawei Wu[‡‡2], and Jinpeng Sun[‡¶¶‖‖3]

From the [‡]Key Laboratory Experimental Teratology of the Ministry of Education, Department of Biochemistry and Molecular Biology, and the [¶]Department of Physiology, Shandong University School of Medicine, Jinan, Shandong 250012, China, the [§]School of Pharmaceutical Sciences, Shandong University, Jinan, Shandong 250012, China, the [‖]School of Life Science, Shandong University, Jinan, Shandong 250003, China, the [**]School of Medicine, Duke University, Durham, North Carolina 27705, the [‡‡]MOE Key Laboratory of Protein Science, School of Life Sciences, Tsinghua University, Beijing 100084, China the [§§]Department of Pharmacology, Hebei Medical University, Shijiazhuang 050017, China, the [¶¶]Department of Physiology and Pathophysiology, School of Basic Medical Sciences, Peking University, Beijing 100191, China, and the [‖‖]Key Laboratory of Molecular Cardiovascular Science, Ministry of Education, Peking University, Beijing 100191, China

Edited by Roger J. Colbran

Slingshots are phosphatases that modulate cytoskeleton dynamics, and their activities are tightly regulated in different physiological contexts. Recently, abnormally elevated Slingshot activity has been implicated in many human diseases, such as cancer, Alzheimer's disease, and vascular diseases. Therefore, Slingshot-specific inhibitors have therapeutic potential. However, an enzymological understanding of the catalytic mechanism of Slingshots and of their activation by actin is lacking. Here, we report that the N-terminal region of human Slingshot2 auto-inhibits its phosphatase activity in a noncompetitive manner. pH-dependent phosphatase assays and leaving-group dependence studies suggested that the N-terminal domain of Slingshot2 regulates the stability of the leaving group of the product during catalysis by modulating the general acid Asp[361] in the catalytic VYD loop. F-actin binding relieved this auto-inhibition and restored the function of the general acid. Limited tryptic digestion and biophysical studies identified large conformational changes in Slingshot2 after the F-actin binding. The dissociation of N-terminal structural elements, including Leu[63], and the exposure of the loop between α-helix-2 and β-sheet-3 of the phosphatase domain served as the structural basis for Slingshot activation via F-actin binding *in vitro* and via neuregulin stimulation in cells. Moreover, we designed a FlAsH-BRET–based Slingshot2 biosensor whose readout was highly correlated with the *in vivo* phosphatase activities of Slingshot2. Our results reveal the auto-inhibitory mechanism and allosteric activation mechanisms of a human Slingshot phosphatase. They also contribute to the design of new strategies to study Slingshot regulation in various cellular contexts and to screen for new activators/inhibitors of Slingshot activity.

Slingshots are a small group of phosphatases that regulate multiple physiological functions, such as axon growth and pathfinding (1–3), neutrophil chemotaxis (4), innate immune responses (5), and mitosis (6, 7), by dephosphorylating cofilin and LIMK[4] to modulate actin dynamics (6). Abnormally increased Slingshot phosphatase activity is found in many human diseases, including cancer (8, 9), salmonella-related diseases (10), and Alzheimer's disease (11), as well as vascular diseases such as aortic aneurysms, atherosclerosis, and post-angioplasty restenosis (12, 13), which is unsurprising, given their role as an important hub controlling actin dynamics. Reducing Slingshot expression or inhibiting Slingshot activity using small chemical compounds has been suggested as a new strategy for treating these diseases (14, 15). Therefore, a comprehensive understanding of the regulation of Slingshot activity and function in different cellular and biochemical contexts will substan-

This work is supported by National Natural Science Foundation of China Grants 31470789, 31611540337, and 81773704 (to J.-P. S.), 31471102 and 31671197 (to X. Y.), and 31700692 (to P. X.); Shandong Natural Science Fund for Distinguished Young Scholars Grant JQ201517 (to J.-P. S.), Shandong Natural Science Fund Grant ZR2016CQ07 (to P. X.); Key Research and Development Program of Shandong Province Grant 2018GSF118147 (to P. X.); Fundamental Research Fund of Shandong University Grant 2016JC017 (to J.-P. S.); China Postdoctoral Science Foundation Grant 2015M582082 (to P. X.); and the Program for Changjiang Scholars and Innovative Research Team in University Grant IRT_17R68 (to X. Y. and J.-P. S). The authors declare that they have no conflicts of interest with the contents of this article.

This article contains Tables S1–S3 and Figs. S1–S11.

[1] These authors contributed equally to this work.

[2] To whom correspondence may be addressed: MOE Key Laboratory of Protein Science, School of Life Sciences, Tsinghua University, Beijing 100084, China. E-mail: jiaweiwu@mail.tsinghua.edu.cn.

[3] To whom correspondence may be addressed: Key Laboratory Experimental Teratology of the Ministry of Education and Department of Biochemistry and Molecular Biology, Shandong University, School of Medicine, Jinan, Shandong 250012, China. E-mail: sunjinpeng@sdu.edu.cn.

[4] The abbreviations used are: LIMK, LIM domain kinase; SSH, Slingshot; NRG, neuregulin-1; PKD, serine/threonine-protein kinase D1; GSK, glycogen synthase kinase; *p*NPP, *p*-nitrophenyl phosphate; DiFMUP, 6,8-difluoro-4-methylumbelliferyl phosphate; OMFP, 3-*O*-methylfluorescein phosphate; rLuc, *Renilla* luciferase; MUP, 4-methylumbelliferyl phosphate; mBBr, monobromobimane; IPTG, isopropyl-1-thio-β-D-galactopyranoside; DMG, 3,3-dimethylglutaric acid; FL, full-length; Ni-NTA, nickel-nitrilotriacetic acid; GST, glutathione *S*-transferase; p-cofilin, phospho-cofilin.

tially help in developing new therapeutic methods targeting this small group of phosphatases.

Slingshots are known to be inactivated by phosphorylation and activated by binding to F-actin (6, 16, 17). In mammals, the Slingshot family contains three members, Slingshot1–3 (SSH1–SSH3). SSH1 and SSH2 are structurally similar and exhibit good activity toward phospho-cofilin (6). In contrast, SSH3 shows minimal C-terminal sequence identity with SSH1 and SSH2 and exhibits very low activity toward phospho-cofilin (6). Whereas phosphorylation of the SSH1 at Ser^{978} by PKD and phosphorylation of the SSH2 on its N-terminal Ser residues by GSK3 dampen their activities toward phospho-cofilin (18, 19), F-actin binding to SSHs significantly increases their phosphatase activities (16). Until now, the detailed enzymological understanding and structural characterization of Slingshot catalysis and activation had not yet been established.

In the current study, we screened a series of SSH1 and SSH2 constructs for expression and purification in *Escherichia coli*. An SSH2-1-490 construct was readily expressed and was purified to homogeneity; the large quantity of the resulting protein facilitated further enzymological and biophysical studies. Our enzymological studies revealed that the N-terminal domain of SSH2 (including a pleckstrin homology–like domain; residues 90–197) serves as an auto-inhibitory module of SSH2 phosphatase activity by modulating a key catalytic step, the stabilization of the product leaving group. Actin binding to Slingshot relieves the auto-inhibitory effect of the Slingshot N-terminal domain. Biochemical analysis using limited tryptic digestion and biophysical studies using the fluorescence spectroscopy enabled us to identify the key structural features, such as a motif encompassing Leu^{63}, in the auto-inhibition of Slingshot phosphatase activity by its N-terminal domain and its subsequent activation after F-actin association. Moreover, the observed conformational changes during Slingshot activation derived from the *in vitro* results enabled us to design FlAsH-BRET probes of full-length Slingshot2 that reveal the structural rearrangement and activity of Slingshot2 in cells in response to neuregulin-1β (NRG) stimulation. This new biosensor will be a useful tool not only for dissecting regulatory mechanisms and functions of Slingshot in different physiological and pathological contexts, but also for potentially contributing to the screening of small compounds that regulate Slingshot activity in an allosteric manner.

Results

Auto-inhibition by the N-terminal domain of Slingshot2

To investigate how regions other than the phosphatase domain contribute to Slingshot catalytic activity, we generated a series of Slingshot2 truncations (Table S1). A construct (SSH2-1-490) encompassing the N-terminal region (Fig. 1*A*), catalytic domain, and an additional 40 amino acids at the C terminus was readily expressed in *Escherichia coli* and purified to homogeneity (Fig. 1*A* and Fig. S1). Five constructs with N- or C-terminal deletions were subsequently generated and assayed for their phosphatase activity toward a variety of substrates (Fig. 1*A*). Stepwise truncation of the N-terminal region caused a gradual increase in SSH2 activity, and the construct with the N terminus deleted (residues 305–490) showed the highest phosphatase activity toward small artificial substrates, including *p*-nitrophenyl phosphate (*p*NPP), 6,8-difluoro-4-methylumbelliferyl phosphate (DiFMUP), and 3-*O*-methylfluorescein phosphate (OMFP), regardless of the number of rings in the substrates or the different pK_a values of the leaving groups (Fig. 1*B* and Table S2). Interestingly, further deletion of the C-terminal 40 amino acids (residues 305–450) slightly decreased SSH2 phosphatase activity toward *p*NPP but significantly decreased activity toward DiFMUP and OMFP, indicating that these residues participate in the recognition of the small multiple ring substrates of SSH2 (Fig. 1*B*).

Importantly, including the N-terminal 232 amino acids or deleting the C-terminal 35 amino acids of SSH2(1–490) impaired its phosphatase activity toward the protein substrate phospho-cofilin *in vitro*, suggesting the auto-inhibitory role of the N-terminal 1–232 region and the essential role for the 455–490 region of SSH2 in phospho-cofilin recognition (Fig. 1*C* and Fig. S4). Notably, the N-terminal 233–304 region is required for SSH2 phosphatase activity toward phospho-cofilin protein but not essential for the recognition of small artificial substrates, indicating that more structural modules are required for protein substrate recognition by Slingshots. Notably, the gel filtration result indicated that the SSH2(1–490) was a monomer (Figs. S2 and S3). Therefore, the above observed auto-inhibitory effect was mainly intramolecular.

We next expressed the SSH2-full-length (SSH2-FL, residues 1–1423) and SSH2(233–1423) (SSH2–233-FL) in HEK293 cells and purified them for an enzymatic assay. The SSH2–233-FL exhibited significantly higher phosphatase activity than the SSH2-FL toward phospho-cofilin, which was abolished by adding the SSH2(1–227) N-terminal fragment (Fig. 1*D*). Taken together, these results revealed an auto-inhibitory role for the N-terminal SSH2(1–232) region with regard to its phosphatase activity toward a variety of substrates.

Noncompetitive inhibition of SSH2 phosphatase activity by its N-terminal region

To dissect the auto-inhibitory mechanism of the N-terminal region toward Slingshot phosphatase activity, we purified the N-terminal 1–227 region of Slingshot and examined its effect on the intrinsic phosphatase activity of SSH2(233–490). Lineweaver–Burk plots indicated that the addition of increasing concentrations of N-terminal SSH2(1–227) had no effect on K_m but significantly decreased V_{max} (Fig. 1*E*, *left*), suggesting noncompetitive inhibition (20, 21). Using *p*NPP as substrate, the K_i for the N-terminal 1–227 region toward SSH2(233–490) was 1.6 μM $\pm$ 0.13. A similar but weaker mode of inhibition by the SSH2(1–227) on the SSH2 catalytic domain (residues 305–490) (K_i was 5.41 $\pm$ 0.37 μM) was also observed (Fig. 1*E*, *right*), suggesting that SSH2(1–227) modulates SSH2 phosphatase activity by directly interacting with key catalytic elements located in the phosphatase domain (residues 305–490), slowing its important hydrolysis steps. The weaker inhibition also suggested that the 1–227 region interacts with the 233–305 region of SSH2. Consistently, the N-terminal 1–227 region of the Slingshot2 exhibited a noncompetitive inhibition mode toward its catalytic domain using physiological substrate phospho-cofilin. K_i was 5.84 μM $\pm$ 0.30 (Fig. 1*F*). A proposed model is illustrated in Fig. 1*G*.

The SSH2 N-terminal domain modulates the stability of the product leaving group during the catalysis

We next carried out enzymology analysis to delineate how the N-terminal domain of SSH2 modulates catalysis. Similar to all other known tyrosine phosphatases, the pH dependence of the SSH2-hydrolyzed *p*NPP reaction follows a bell-shaped curve, suggesting the involvement of a general acid–base catalytic mechanism (Fig. 2, *A* and *B*). The pH-independent maximum first-order rate $(k_{cat})^{lim}$ and second-order rate constants $(k_{cat}/K_m)^{lim}$ of SSH2, which are more accurate measurements of intrinsic SSH2 phosphatase activity, were on the order of SSH2(305–490) > SSH2(233–490) > SSH2(1–490) (Fig. 2, *A* and *B*). Moreover, the basic limbs (pH >6) of both of the k_{cat} and the k_{cat}/K_m of SSH2(1–490) were much shallower than those of SSH2(233–490) and SSH2(305–490) (Fig. 2, *A* and *B*), suggesting that the N-terminal domain of SSH2 might involve in the breaking of the P–O bond.

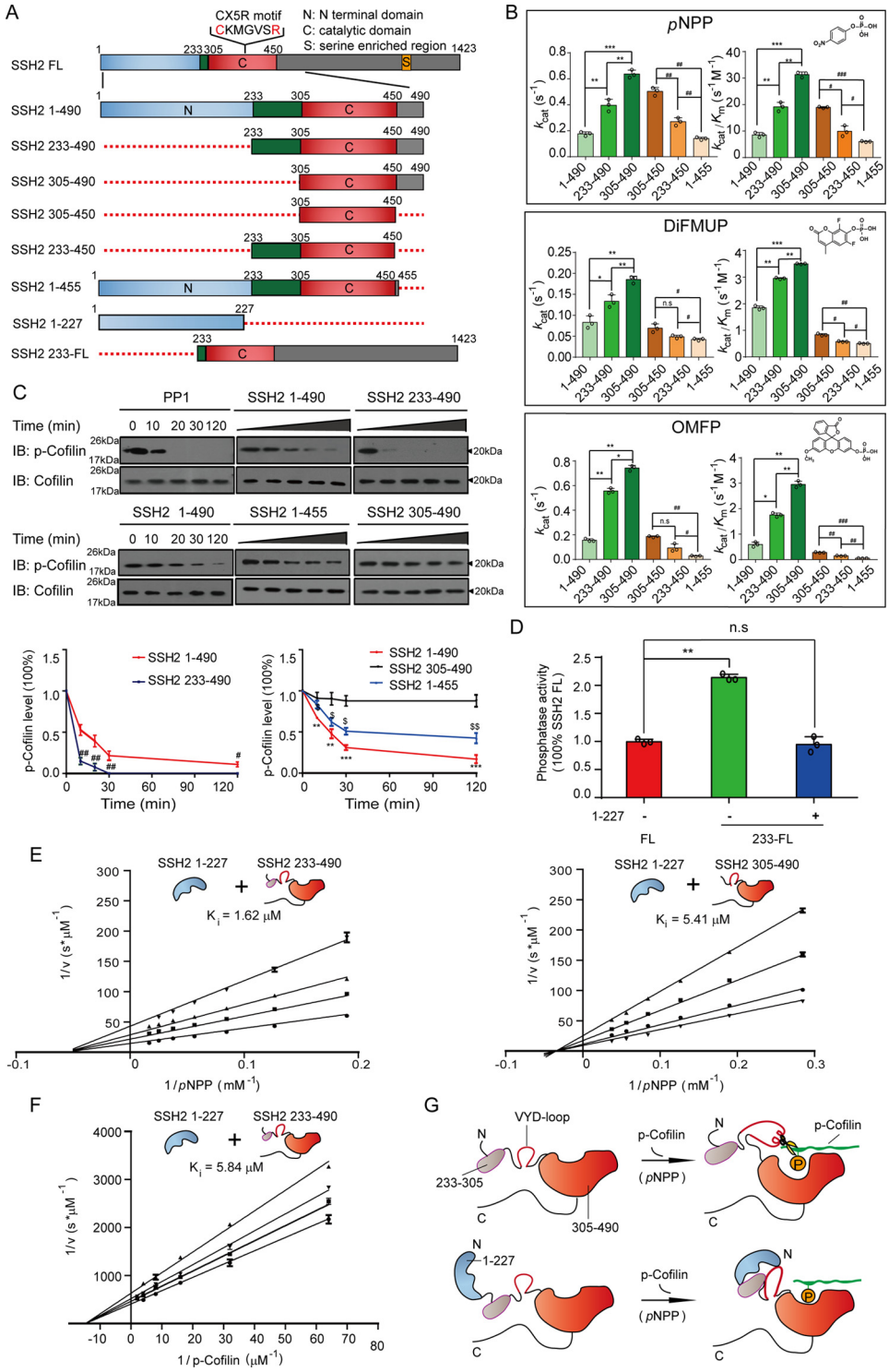

During tyrosine phosphatase catalysis, a conserved general acid was identified in most PTP members to stabilize the negative charge developed on the leaving-group phenol-OH after breakage of the P–O bond by nucleophilic attack of the catalytic cysteine. All three SSH members contain a conserved VYD loop, which is structurally equivalent to the classic WPD loop of tyrosine phosphatases and harbors the general acid (Asp^{361} in SSH2). Protonation of Asp^{361} in SSH2 is predicted to form a hydrogen bond with the phenolic oxygen of the product, a key step for efficient substrate hydrolysis that appears as the basic limb on the pH-dependence curve. The difference in the basic limb of the pH-dependence curve suggested a less effective general acid function in SSH2(1–490) than in the truncation SSH2(233–490). We therefore used Brønsted plots to investigate the effect of the SSH2 N-terminal domain on the general acid catalysis by measuring the dependence of catalysis on the characteristics of the leaving group (22) (Fig. 2, *C* and *D*). Whereas the β_{1g} values for both k_{cat} and k_{cat}/K_m are very similar in SSH2(233–490) and SSH2(305–490), the β_{1g} value for SSH2(1–490) is significantly lower, confirming the impaired general acid catalysis for the intrinsic activity and the reduced stability of the leaving group during the catalytic process of SSH2(1–490).

F-actin activates SSH2 through relieving auto-inhibition by its N-terminal domain

Although full-length Slingshot exhibited relatively low phosphatase activity toward both small artificial substrates and its physiological substrate phospho-cofilin, a dramatic increase in Slingshot activity has previously been observed following incubation with F-actin (16). The N-terminal Arg^{96}, the Leu^{185}–Lys^{187} region, and the C-terminal Trp^{457} of SSH1 were identified as being directly involved in actin binding (16, 24). We therefore examined the effect of actin on the phosphatase activity of different SSH2 truncations. Incubation with 4 μM F-actin markedly increased the dephosphorylation of phospho-cofilin by SSH2(1–490) but has little effect on SSH2(233–490) or SSH2(305–490) (Fig. 3, *A* and *B*). Similarly, incubation of F-actin significantly improved the activity of SSH2(1–490) and SSH2(1–455) toward *p*NPP, the two constructs encompassing residues 1–232, but had little effect on SSH2(233–490), SSH2(305–490), SSH2(305–450), or SSH2(233–450) (Fig. 3*C*). In particular, the intrinsic activity of SSH2(1–490) in the presence of F-actin was approximately the same as that of SSH2(233–490) toward *p*NPP. These data suggested that the binding of F-actin disabled the auto-inhibitory function of the SSH2 N-terminal domain.

We then examined the effect of actin on the leaving-group dependence of SSH2-catalyzed *p*NPP hydrolysis using Brønsted plots. Interestingly, the slope of the Brønsted plot was much shallower in the presence of actin than the plot of SSH2(1–490) alone (Fig. 3, *D* and *E*). The β_{1g} values for the k_{cat}/K_m and k_{cat} of SSH2(1–490) in the presence of the actin were −0.08 and −0.23, respectively, similar to those for SSH2(233–490) and much higher than the β_{1g} value of SSH2(1–490) alone, suggesting a functional role of restoring the function of the general acid by F-actin association during SSH2 catalysis (Fig. 3*F*). These results suggested that the binding of actin relieves the auto-inhibitory role of the SSH2 N-terminal domain and restores general acid function during catalysis (Fig. 3*G*) (25).

F-actin association leads to SSH2 conformational rearrangements

To investigate the structural basis of SSH2 activation by actin, we next employed limited tryptic proteolysis to monitor conformational changes in SSH2 after association with actin. In general, protein conformational changes will mask or unmask trypsin cleavage sites that produce different trypsin digestion patterns. Because trypsin only recognizes and cleaves proteins at the carbonyl site after Arg or Lys residues, analysis of tryptic digestion patterns has been used to glean structural information in many biochemical studies (26–28). As illustrated in Fig. 4*A*, SSH2(1–490) appeared at 68 kDa, and tryptic digestion produced bands with apparent molecular masses of 40 and 28 kDa. Following incubation with F-actin, a new fragment of SSH2 appeared at 44 kDa, and the 28 and 40 kDa bands were not generated (Fig. 4, *A* and *B*). Moreover, limited trypsin digestion patterns of SSH2(1–490) and SSH2(1–455) were identical, sug-

Figure 1. The noncompetitive auto-inhibitory role of the SSH2 N-terminal domain. *A*, *schematic diagram* showing FL SSH2 and truncated fragments used for enzymology analysis. SSH2 consists of an N-terminal domain (*N*, *blue*), a catalytic domain (*C*, *red*), and a relatively long C-terminal region (*gray*) with a serine-enriched area (*S*, *orange*). *B*, catalytic activity of different SSH2 truncations toward small-molecule aryl phosphate substrates. All kinetic assays using *p*NPP (*top*), DIFMUP (*middle*), and OMFP (*bottom*) as substrates were performed at 30 °C in 50 mM DMG buffer, pH 7.0, containing 1 mM DTT, 1 mM EDTA and adjusted to an ionic strength of 0.15 M with sodium chloride. *, $p < 0.05$; **, $p < 0.01$; ***, $p < 0.005$; #, $p < 0.05$; ##, $p < 0.01$; ###, $p < 0.005$; *n.s.*, no significance. *C*, catalytic activity of different SSH2 truncations for time-dependent hydrolysis of the physiological protein substrate p-cofilin. p-cofilin (0.06 mM) and phosphatases (0.2 μM) were mixed in 20 mM Tris buffer (pH 7.0) containing 100 mM NaCl, 1 mM DTT, and 1 mM EDTA and incubated at 30 °C for 2 h. Samples were taken at the indicated time points and analyzed by Western blotting using antibodies against Ser^3-phosphorylated cofilin or total cofilin (*left*). Cofilin phosphorylation levels were quantified and expressed as percentages of total cofilin (*right*). PP1 served as a positive control. #, $p < 0.05$; ##, $p < 0.01$; **, $p < 0.01$; ***, $p < 0.005$; p-cofilin levels in SSH2(1–490)–treated samples compared with those in SSH2(305–490)–treated samples. *D*, phosphatase activities of SSH2-FL(1–1423) and SSH2–233-FL(233–1423) toward p-cofilin protein *in vitro* with or without SSH2(1–227). SSH2(1–1423) and SSH2(233–1423) with a His_6 tag at the N terminus were transfected into MCF-7 cells. The Slingshots were then purified by Ni-NTA beads and gel filtration. The initial p-cofilin concentration was 2 μM, and Slingshots were 0.15 μM. SSH2(1–277) (0.8 μM) and SSH2(233–1423) were incubated for 1 h before the reactions began. The reactions were terminated by Biomol Green reagent, and an P_i assay was used to determine the released phosphate. *E*, Lineweaver–Burk plot of the phosphatase activity of SSH2 catalytic domain (residues 233–490 and 305–490) toward small artificial substrate *p*NPP incubated with different concentrations of the N-terminal domain (residues 1–227). The initial rate at different *p*NPP concentrations (K_m 0.2–5) was measured at 25 °C, pH 7.0, in a reaction mixture containing 0.5 μM SSH2(233–490) (*top left*) or SSH2(305–490) (*top right*) and SSH2(1–227) at a series of fixed concentrations. SSH2(1–227) concentrations were 0 (▲), 1.2 (▼), 4.8 (●), and 9.6 μM (■) (*left*) and 0 (▲), 0.8 (▼), 1.6 (●), and 3.2 μM (■) (*right*). The inhibition constant K_i and inhibition pattern were evaluated by fitting the data to the Michaelis–Menten equation. *F*, Lineweaver–Burk plot of the phosphatase activity of SSH2(233–490) toward phospho-cofilin protein incubated with different concentrations of the N-terminal domain (residues 1–227). The initial rates at different p-cofilin concentrations from 0.02 to 2 μM were measured at 30 °C, pH 7.0. SSH2(1–227) concentrations were 0 (▲), 0.8 (▼), 1.6 (●), and 3.2 μM (■) (*bottom left*). The dephosphorylation was measured by a P_i assay using Biomol Green. *G*, a schematic description of the auto-inhibitory role of the SSH2 N-terminal domain (SSH2(1–227)), which functions as a noncompetitive inhibitory element for SSH2 phosphatase activity. In all panels, data are given as the mean ± S.E. (*error bars*) of three independent experiments, and *p* values were determined by *t* tests.

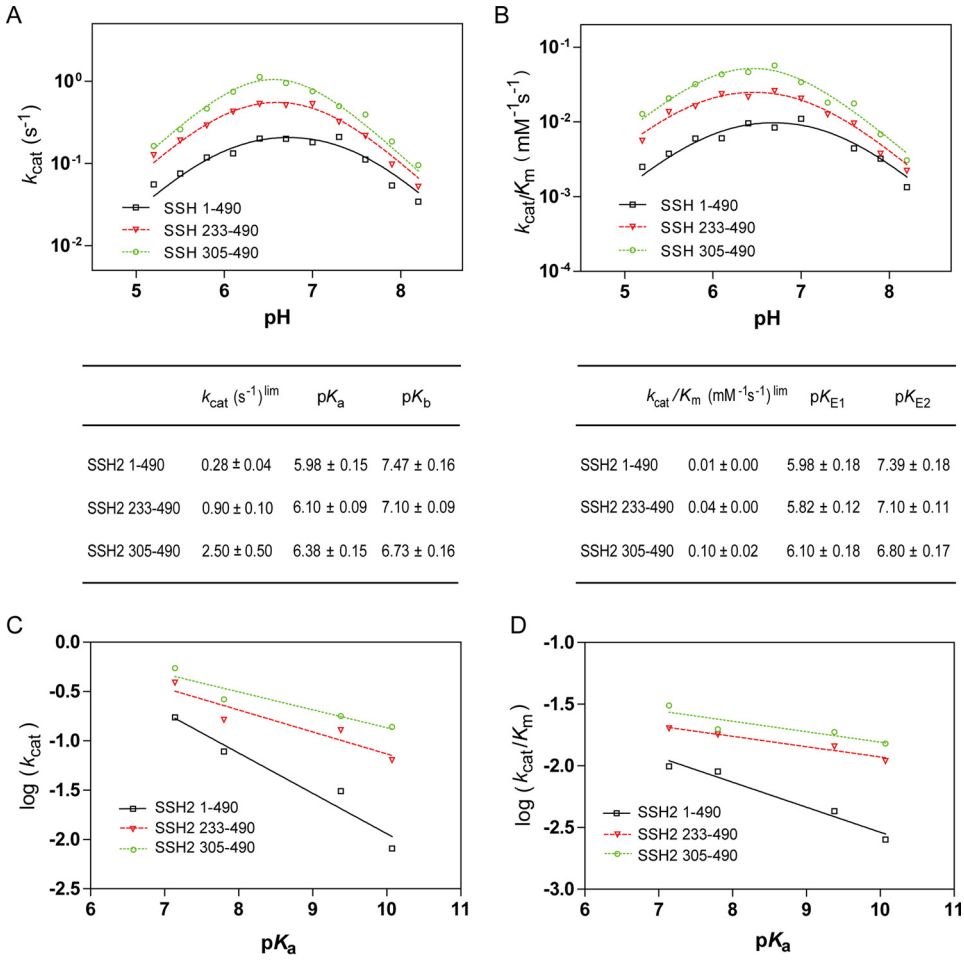

	k_{cat} (s^{-1})^{lim}	pK_a	pK_b
SSH2 1-490	0.28 ± 0.04	5.98 ± 0.15	7.47 ± 0.16
SSH2 233-490	0.90 ± 0.10	6.10 ± 0.09	7.10 ± 0.09
SSH2 305-490	2.50 ± 0.50	6.38 ± 0.15	6.73 ± 0.16

	k_{cat}/K_m ($mM^{-1}s^{-1}$)^{lim}	pK_{E1}	pK_{E2}
SSH2 1-490	0.01 ± 0.00	5.98 ± 0.18	7.39 ± 0.18
SSH2 233-490	0.04 ± 0.00	5.82 ± 0.12	7.10 ± 0.11
SSH2 305-490	0.10 ± 0.02	6.10 ± 0.18	6.80 ± 0.17

	β_{1g} (k_{cat})	β_{1g} (k_{cat}/K_m)
SSH2 1-490	-0.41 ± 0.06	-0.20 ± 0.02
SSH2 233-490	-0.22 ± 0.06	-0.08 ± 0.01
SSH2 305-490	-0.18 ± 0.04	-0.08 ± 0.03

Figure 2. pH dependence and leaving-group dependence of different SSH2 truncations in catalyzing aryl phosphate hydrolysis. The K_{cat}/K_m *versus* pH (*A*) and K_{cat} *versus* pH (*B*) profiles for SSH2(1–490) (□), SSH2(233–490) (▽), and SSH2(305–490) (○)–catalyzed hydrolysis of *p*NPP were measured at 30 °C in 50 mM succinate (pH 5.0–6.5), DMG (pH 6.6–7.5), or Tris (pH 7.5–8.5) buffered reaction mixtures (*top*). The *fitted bell-shaped curves* were calculated using Equation 4 for the k_{cat} profiles and using Equation 3 for the k_{cat}/K_m profiles. The kinetic parameters of k_{cat}^{lim}, pK_a, and pK_b and pK_{E1}, pK_{E2}, and $(k_{cat}/K_m)^{lim}$ were generated with the data presented in the *top panel* (*bottom*). Leaving-group dependence of K_{cat} (*C*) and K_{cat}/K_m (*D*) for SSH2(1–490) (□), SSH2(233–490) (▽), and SSH2(305–490) (○) was determined at 30 °C in 50 mM DMG buffer, pH 7.0, using *p*NPP (pK_a = 7.14), 4-methylumbelliferyl phosphate (pK_a = 7.80), β-naphthyl phosphate (pK_a = 9.38), and *O*-phospho-L-tyrosine (pK_a = 10.07) as substrates. The *lines* were generated by linear least-squares fitting to a plot of log(K_{cat}) (*C*) and log(K_{cat}/K_m) (*D*) *versus* leaving-group pK_a. *E*, the β_{1g} values for K_{cat} and K_{cat}/K_m of different SSH2 truncations were obtained by fitting Brønsted plots from *C* and *D*. All values were obtained from three independent experiments, and the data are expressed as the mean ± S.E. (*error bars*).

gesting that digestion at Lys^{450} occurred at the C terminus in both constructs (Fig. 4, *C* and *D*). Mapping of the Arg and Lys positions indicated that SSH2 alone was cleaved by trypsin at Arg^{66}, Lys^{291}, and Lys^{450}, whereas SSH2 incubated with actin was mainly cleaved at Arg^{66} and Arg^{332} (Figs. S5 and S6). Taken together, these results suggested that the linker region (residues 233–304) between the N-terminal auto-inhibitory domain and the phosphatase domain, which encompasses Lys^{291}, is more accessible by trypsin in SSH2(1–490) and is protected after F-actin association. In contrast, the loop between α-helix-1 and β-sheet-3 of the phosphatase domain is protected in SSH2 (1–490) alone (Fig. S6) and is exposed to trypsin after F-actin binding (Fig. 4, *E* and *F*). These conformational changes are remote from the active site of the Slingshot catalytic domain, consistent with the noncompetitive inhibition of Slingshot by its N-terminal domain and subsequent activation by an allosteric mechanism. Taken together, these results indicate significant conformational changes after association of actin with SSH2(1–490), including the protection of the linker region between the N-terminal domain and the phosphatase domain and the exposure of the loop between α-helix-2 and β-sheet-3 of the phosphatase domain (Fig. 3*G* and Fig. S6).

F-actin activates SSH2 by specifically modulating the interaction of the N-terminal region of SSH2 with the VYD loop

Enzymology studies indicated that actin activated SSH2 phosphatase activity by modulating the general acid catalytic process. By examining the available SSH2 crystal structure (29), the general acid of the SSH2 is likely residue Asp^{361} (Fig. S7), which is located in the VYD loop of the SSH2 phosphatase domain. To further dissect the structural basis of how actin binding regulates SSH2 activity by modulating the VYD loop, we generated a series of modified SSH2(1–490) fluorescence reporters and utilized the bimane-tryptophan technique (30, 31) along with fluorescence spectroscopy to monitor confor-

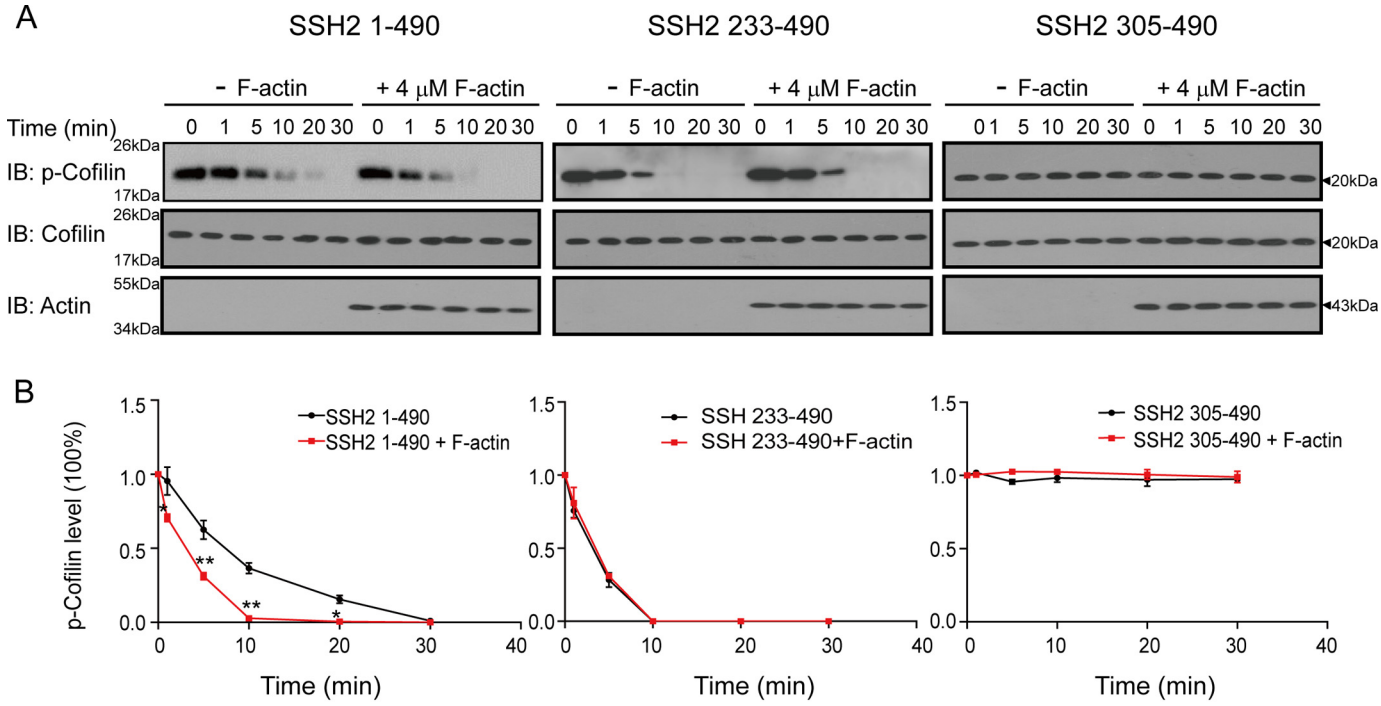

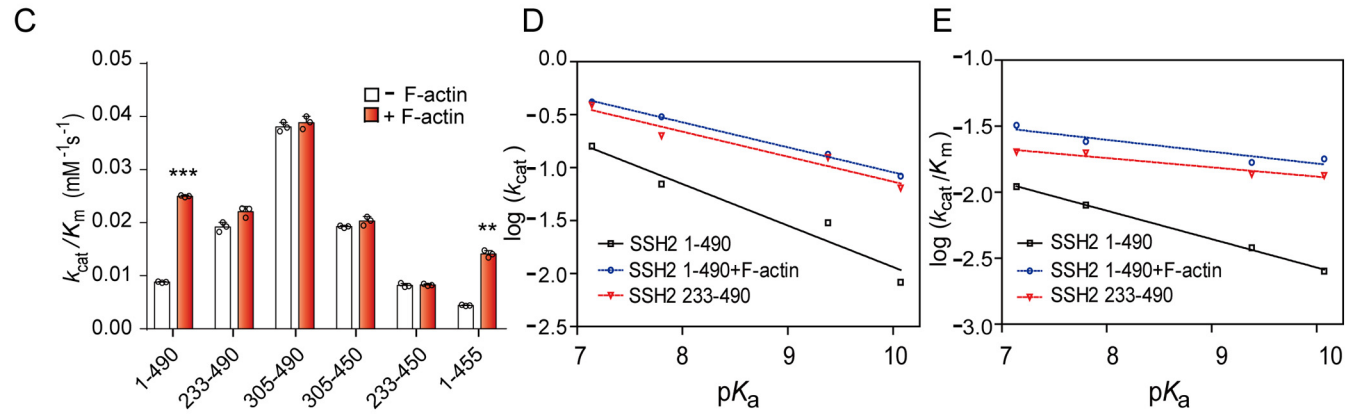

F

	β_{1g} (k_{cat}/K_m)	β_{1g} (k_{cat})
SSH2 1-490	-0.21 ± 0.01	-0.39 ± 0.01
SSH2 1-490 + F-actin	-0.08 ± 0.02	-0.23 ± 0.01
SSH2 233-490	-0.07 ± 0.01	-0.24 ± 0.04

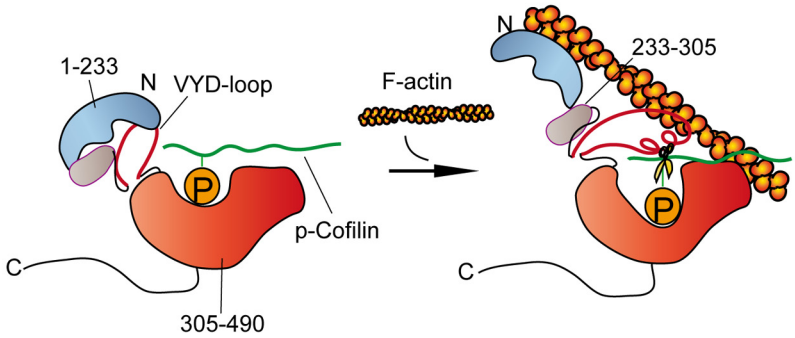

mational changes in SSH2 after incubation with F-actin. Mutating all Cys residues to Ser other than the catalytic Cys^{392} had no effect on intrinsic phosphatase activity (Fig. S8*A*), suggesting that these mutations do not perturb the structural integrity of SSH2(1–490). We therefore introduced specific cysteines in the N terminus of SSH2 into a minimal-cysteine SSH2(1–490) background (Fig. 5*A*) and specifically labeled these single cysteines with monobromobimane. The labeled Slingshot proteins were subsequently purified with GSH-Sepharose 4B to remove unbound bimane, and SDS-PAGE was used to monitor protein purity (Fig. S9). No substitutions or labeling affected phosphatase activity (Fig. S8*B*).

We next introduced a Y360W mutation in the VYD loop of SSH2 to monitor its interaction with the six bimane probes located in the N-terminal region of SSH2 (Fig. S10). Significant decreases in the fluorescence of SSH2–63C-bimane (18%), SSH2–78C-bimane (43%), SSH2–98C-bimane (25%), and SSH2–161C-bimane (34%) were observed after introduction of the Y360W mutation; SSH2–19C-bimane and SSH2–146C-bimane showed no significant fluorescence changes (Fig. 5*B*). These results indicated that Cys^{19} and Cys^{146} are far from the VYD loop, whereas Cys^{63}, Cys^{78}, Cys^{98}, and Cys^{161} are near the VYD loop in the resting state of SSH2, probably less than 10 Å away, a suitable distance for the detection of fluorescence quenching.

We then examined the effect of F-actin binding on fluorescence spectroscopy using SSH2-fluorescence probes (Fig. 5, *B–E*). Whereas incubating F-actin with SSH2–78C-bimane-Y360W, SSH2–98C-bimane-Y360W, or SSH2–146C-bimane-Y360W had no significant effect on their fluorescence spectra, incubating F-actin with SSH2–63C-bimane-Y360W and SSH2–161C-bimane-Y360W increased their fluorescence intensity by 30 and 12%, respectively. Notably, the addition of F-actin to SSH2–63C-bimane caused a decrease rather than an increase in fluorescence intensity, such as in SSH2–161C-bimane. Therefore, the increase in the fluorescence intensity of SSH2–63C-bimane-Y360W reflects the specific dislodging of Cys^{63} from the VYD loop after F-actin association. In contrast, although incubating actin with SSH2–19C-bimane caused no significant change in fluorescence intensity, the fluorescence intensity of SSH2–19C-bimane-Y360W decreased significantly, suggesting that F-actin binding brought Cys^{19} into close proximity with the VYD loop.

Taken together, the fluorescence spectroscopy results suggested that Cys^{19} and Cys^{146} are distal to the VYD loop, whereas Cys^{63}, Cys^{78}, Cys^{98}, and Cys^{161} are close by in the resting state. Upon F-actin association, a structural element encompassing Cys^{63} moves away from the VYD loop, whereas a structural segment containing Cys^{19} moves closer to the VYD loop. Thus, specific conformational rearrangements, including the association and dissociation of specific structural elements that participate in coordinating VYD loop function for effective catalysis, underlie the activation of Slingshot phosphatase activity by F-actin *in vitro* (Fig. 5*F*).

A conformational biosensor for Slingshot2 indicates allosteric activation of this protein in cells

To extend our hypotheses regarding the inhibition of Slingshot by its N-terminal domain in a resting state and the release of its N terminus from the VYD loop after subsequent activation in a more physiological context, we prepared a series of FlAsH-BRET probes (32) for Slingshot2 by inserting the six-amino acid motif CCPGCC and the donor *Renilla* luciferase (rLuc) into full-length Slingshot2 and expressed the resulting modified proteins in MCF-7 cells (Fig. 6*A*). The FlAsH motif was incorporated into the catalytic VYD loop of full-length Slingshot2, and we assumed that the observed changes in the efficiency of BRET signaling between FlAsH and the inserted rLuc would yield a conformational signature indicating the relationship between the probe's VYD loop and specific positions in the N terminus in a cellular context (Fig. 6*A*). Both FlAsH-BRET probes (SSH2–23-FlAsH and SSH2–63-FlAsH) retained their functional integrity; in particular, both probes promoted cofilin dephosphorylation to a similar extent as that observed for WT Slingshot2 in response to NRG stimulation (Fig. 6, *B–D*). These probes consistently exhibited similar phosphatase activities toward the substrates *p*NPP and phosphocofilin *in vitro* (Fig. S11, *A–D*). We then tested whether NRG stimulation produced a conformational change in Slingshot2 that could be captured by intramolecular rLuc-Slingshot2-FlAsH BRET signals from the two probes based on biochemical results. Intriguingly, NRG treatment induced an increase in the BRET signal from SSH2–23-FlAsH and a decrease in the BRET signal from SSH2–63-FlAsH, suggesting that residue 23 moves closer to the catalytic VYD loop of the Slingshot2 but that residue 63 moves away from this catalytic structure; these findings exhibit good agreement with observations of conformational changes of allosteric activation of Slingshot2 *in vitro* (Figs. 5*F* and 6*D*).

Based on these consistent findings that the N-terminal region of Slingshot2 that includes position 63 moved away from the catalytic VYD loop, we postulated that SSH2–63-FlAsH could be used to report Slingshot2 activity changes in cells. As expected, the ΔBRET values determined using SSH2–63-

Figure 3. Relieving the auto-inhibition of the SSH2 N-terminal domain by F-actin binding. *A* and *B*, F-actin activates SSH2(1–490) catalytic activity toward p-cofilin. *A*, representative Western blotting analyses (*IB*) of time-dependent p-cofilin hydrolysis by different SSH2 truncations. Truncations of SSH2 (0.4 μM) were preincubated with or without 4 μM F-actin in activation buffer containing 20 mM Tris-HCl, pH 7.0, and 100 mM NaCl at 25 °C for 1 h. p-cofilin was then added to the reaction to a final concentration of 60 ng/μl and incubated for the indicated times. Aliquots were subjected to SDS-PAGE followed by immunoblotting using specific antibodies against $pSer^3$-cofilin, total cofilin, and actin. *Numbers* indicate the time (min) of each reaction. *B*, quantification and statistical analysis of Western blots, shown as the percentage of total cofilin. *C*, F-actin activates SSH2(1–490)– catalyzed *p*NPP hydrolysis. The values of the kinetic parameter K_{cat}/K_m for SSH2-catalyzed hydrolysis of *p*NPP with or without F-actin (0.4 μM) were compared. *D* and *E*, F-actin binding relieves the dependence of SSH2(1–490) K_{cat} (*D*) and K_{cat}/K_m (*E*) on the leaving-group pK_a of aryl phosphate substrates. SSH2(1–490) (0.4 μM) was pre-incubated with (□) or without (○) 4 μM F-actin in activation buffer, and then *p*NPP ($pK_a = 7.14$), 4-methylumbelliferyl phosphate ($pK_a = 7.80$), β-naphthyl phosphate ($pK_a = 9.38$), and *O*-phospho-L-tyrosine ($pK_a = 10.07$) were added for activity determination. *F*, the β_{1g} values were obtained by fitting Brønsted plots from Fig. 5 (*D* and *E*). *G*, a speculated schematic description of the relief of auto-inhibition by the SSH2 N-terminal domain upon F-actin binding. F-actin binding relieves auto-inhibition by the SSH2 N-terminal domain, resulting in substrate access to the catalytic site. For all statistical analyses, data from at least three independent experiments were quantified and presented as the mean ± S.E. (*error bars*). *, $p < 0.05$; **, $p < 0.01$; ***, $p < 0.005$.

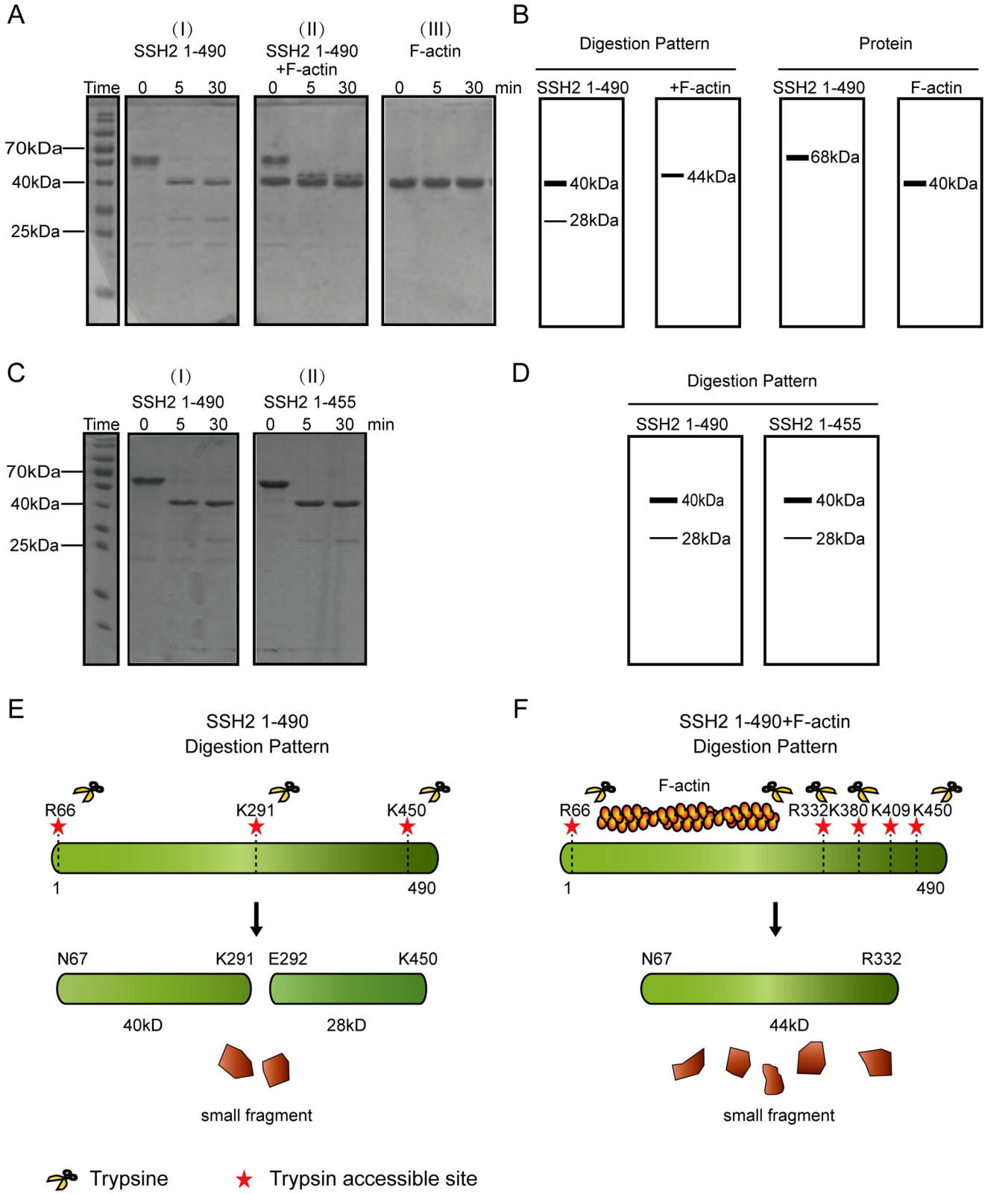

Figure 4. Limited tryptic proteolysis reveals F-actin–induced conformational rearrangements of SSH2. *A*, SDS-PAGE analysis of a time course (min) of limited tryptic proteolytic fragments of SSH2(1–490) in the absence (*I*) or presence (*II*) of F-actin and of F-actin alone (*III*). *B*, schematic representation of typical limited tryptic proteolysis profiles in *A*. *C*, SDS-PAGE analysis of limited tryptic fragments of SSH2(1–490) and SSH2(1–455). *D*, schematic representation of typical limited tryptic profiles in *C*. In *A* and *C*, trypsin was incubated with SSH2 or F-actin–activated SSH2 at a ratio of 1:1000 (w/w) in 20 mM Tris, pH 7.0, 100 mM NaCl at 37 °C for the indicated times. Aliquots (~2 μg of protein sample) were subjected to SDS-PAGE. *E* and *F*, schematic description of F-actin activation leading to SSH2 conformational rearrangements. In the case of SSH2(1–490) alone (*E*), the initial tryptic proteolysis generated two relatively large fragments with molecular mass of 40 and 28 kDa, respectively. F-actin binding leads to SSH2 conformational rearrangements, with the exposure of multiple accessible trypsin cleavage sites (*F*), which is responsible for the generation of only one visible fragment ~4 kDa larger than the corresponding fragment formed by digestion of SSH2(1–490) in the absence of F-actin.

FlAsH exhibited dose dependence and were well correlated with cofilin dephosphorylation levels in response to NRG stimulation ($R^2 = 0.9$; Fig. 6 (*E–G*) and Fig. S11*E*). This strong linear correlation between ΔBRET and Slingshot2 activity indicated that SSH2–63-FlAsH served as an effective reporter of Slingshot activity in response to allosteric regulation in cells treated

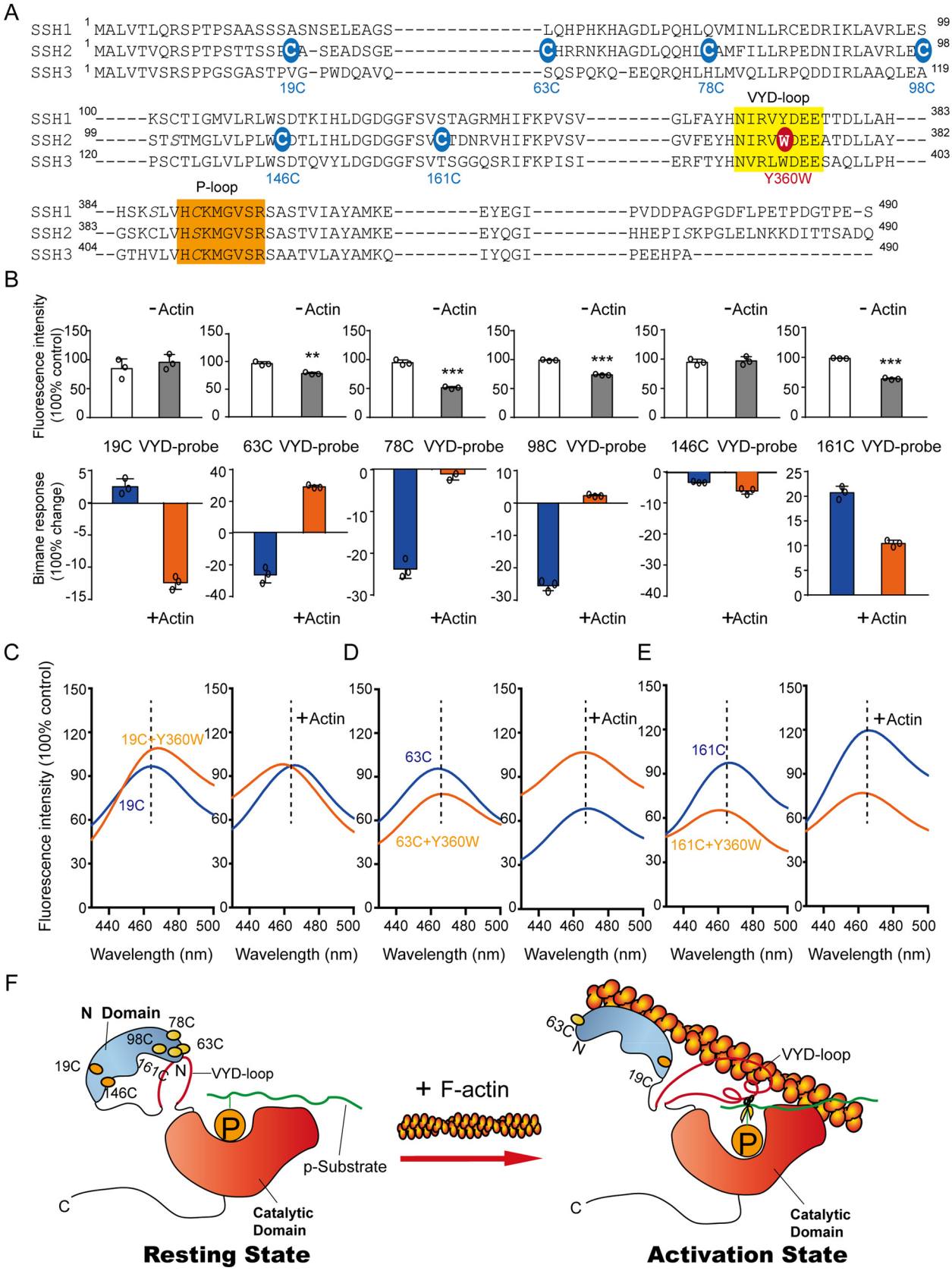

with NRG. A previous report (19) has indicated that the Ser^{21}, Ser^{25}, Ser^{32}, and Ser^{36} in the N-terminal region of SSH2 were phosphorylated by GSK3β, which attenuated the activity of SSH2 toward dephosphorylation of phospho-cofilin. To extend our identified structural alteration and auto-inhibitory mechanism of SSH2 in this specific cellular context, we mutated the Ser^{21} and Ser^{25} to Asp and Ser^{32} and Ser^{36} to Glu to create an SSH2-DDEE phosphomimetic mutant. In response to NRG treatment, the SSH2-DDEE-63-FlAsH ΔBRET signal was significantly lower compared with the SSH2–63-FlAsH (Fig. 6*H*). This result suggested that the inhibitory mechanism of SSH2 phosphorylated by GSK in the N-terminal SSH2 Ser^{21}-Ser^{25}-Ser^{32}-Ser^{36} residues was potentially due to the locking of the SSH2 in an auto-inhibitory mechanism, impairing its ability to dislodge the N-terminal region from the catalytic site in response to actin binding.

Discussion

The reversible regulation of protein phosphorylation states is coordinated by two groups of enzymes, protein kinases and protein phosphatases. Although auto-inhibition and subsequent allosteric activation serve as important regulatory mechanisms for many protein tyrosine kinases to achieve their precise function in different cellular contexts (33–35), few protein phosphatases are known to possess an auto-inhibitory mechanism (36, 37). Whereas recently we have identified the allosteric inhibition of calcineurin by structural studies (36), the best-characterized tyrosine phosphatase with an auto-inhibitory mechanism is SHP2, an important oncogenic PTP involved in Noonan syndrome and other types of cancers (21, 37–40). Similar to SHP2, activation of Slingshots promotes cell motility (6, 21, 41). Therefore, an auto-inhibitory mechanism is important to retain low phosphatases activity in the resting state, and abnormal activation of these phosphatases is related to the progression of diseases such as cancers (9, 21, 37).

In contrast to SHP2, whose N-terminal SH2 domain inserts into the catalytic center and competitively inhibits phosphatase activity (21, 40), here we found that the N-terminal domain inhibited SSH2 in a noncompetitive manner. Our enzymological studies showed that the N-terminal domain inhibited SSH2 activity by modulating the stability of the product leaving group, an important catalytic step that requires the general acid Asp^{361} in the VYD loop of Slingshot. Adding F-actin relieved this auto-inhibition, and biophysical studies suggested that a large conformational change underlies F-actin–mediated SSH2 activation. Therefore, Slingshot activity is regulated by F-actin through delicate structural arrangements, which may account for its exceptional substrate specificity.

Previous studies found that the N-terminal regions are required for F-actin–mediated Slingshot activation and that residues Arg^{96}, Leu^{185}, His^{186}, Lys^{187}, and Trp^{457} of SSH1 may directly interact with F-actin (16, 24). Our biophysical studies found that the 98-C-bimane probe underwent significant fluorescence quenching after incubation with F-actin, confirming that the loop between the β1 and β2 sheets of the predicted PH-like domain (42) is one of the critical interaction sites of Slingshot with F-actin. Moreover, fluorescence spectroscopy revealed that the N-terminal region encompassing Leu^{63} is not only proximal to the VYD loop of SSH2 in the resting state but also a potential docking site for F-actin binding. After F-actin binding, Leu^{63} becomes dislodged from the VYD loop of SSH2. Therefore, the structural motif harboring Leu^{63} may be a determinant for Slingshot activation by inhibiting SSH2 activity through its interaction with the VYD loop in the resting state and subsequent dissociation from the VYD loop following F-actin binding. Importantly, consistent with the aforementioned findings, the release of a segment encompassing Leu^{63} of the Slingshot N terminus from the catalytic VYD in response to NRG stimulation was verified in cells. Moreover, we developed a biosensor that reflects Slingshot2 activity and conformational changes associated with allosteric regulation. This type of biosensor could serve as an important tool to investigate the activation mechanism of Slingshot in different physiological and pathological processes. For example, the phosphorylation of SSH2 in its N-terminal by GSKs was known to attenuate its activity toward phospho-cofilin. Using our FlAsH BRET assay, we were able to dissect the mechanism underlying this specific cellular event. These results indicated that the phosphorylation of SSH2 by GSK3 locked SSH2 in an auto-inhibitory configuration, impairing the dislodging of the N-terminal region of SSH2 from its catalytic site in response to activation.

Recently, an allosteric SHP2 inhibitor was identified that concurrently targets the interface of both the N-terminal inhibitory domain and phosphatase domain and was shown to exhibit strong therapeutic potential (21). Therefore, an inhibitor targeting both the N-terminal Leu^{63} region and the VYD loop of Slingshot is conceivable to drive the development of novel allosteric Slingshot inhibitors. A fluorescence assay that utilizes our newly developed L63C-bimane and L63C-bimane-Y360W probes or a BRET assay with our SSH2–63-FlAsH biosensor may also be useful to screen for allosteric Slingshot regulators.

In conclusion, we have shown that the N-terminal region of Slingshot plays an auto-inhibitory role via allosteric regulation of the catalytic VYD loop and restriction of the stability of the

Figure 5. Structural basis of SSH2 auto-inhibition and activation revealed by steady-state fluorescence spectra. *A*, alignment of the amino acid sequences of SSH subfamily members (*Homo sapiens*). Residues *shaded yellow* and *orange* indicate the VYD loop and P loop, respectively, which are essential for SSH2 phosphatase activity. Single cysteine variants of SSH2 were generated for mBBr labeling. Residues *shaded blue* indicate single specific cysteine sites for mBBr labeling. For steady-state fluorescence analysis, the SSH2 Y360W mutation located in the VYD loop is *highlighted* in *red*. *B*, screening analyses of F-actin–induced conformational changes of mBBr-labeled SSH2(1–490) single-cysteine variants labeled with mBBr coupled to its Y360W mutant. From *left* to *right* are shown SSH2(1–490) single cysteines at positions 19, 63, 78, 98, 146, and 161 labeled with mBBr. *C–E*, representative fluorescence emission spectra of the mBBr-labeled SSH2(1–490) single-cysteine variant (*blue spectra*) and its Y360W mutant (*orange spectra*) in the absence (*left*) or presence (*right*) of F-actin. Shown are fluorescence spectra of mBBr-labeled SSH2(1–490) at positions 19 (*C*), 63 (*D*), and 161 (*E*). *F*, proposed model illustrating that F-actin activates SSH2 by dislodging the auto-inhibitory N-terminal domain from its interaction with the VYD loop. In the resting state, the SSH2 N-terminal domain (*cyan*) lies proximal to the catalytic domain (*red*), where residues 63 and 161 are close to the VYD loop. Upon F-actin activation, the SSH2 N-terminal domain is dislodged from the catalytic domain, causing residues 63 and 161 to move away from the VYD loop and relax it for catalytic activity. *Error bars*, S.E.

leaving group of the product during catalysis in the resting state. Movement of the segment encompassing Leu[63] away from the VYD loop is important for the allosteric activation of Slingshot2 both *in vitro* due to F-actin binding and in cellular contexts in response to NRG stimulation. A fluorescence assay *in vitro* and a BRET assay in cells were developed; these assays could be used to dissect regulatory mechanisms of Slingshot proteins in various contexts or to screen for allosteric Slingshot inhibitors or activators.

Experimental procedures

Materials

*p*NPP, DiFMUP, and 4-methylumbelliferyl phosphate (MUP) were ordered from Sangon Biotech Co. Ltd. (Shanghai, China). 2-Naphthyl phosphate sodium salt, *O*-phospho-L-tyrosine, and OMFP were purchased from Sigma. pSer-cofilin, pThr-cofilin, pThr-LIMK, and all other pTyr-containing peptides were synthesized by China Peptides Co. Ltd. (Shanghai, China) as described previously (43–45). The Biomol Green reagent for terminating enzyme activities was ordered from Enzo Life Sciences (catalogue no. AK111-1000). The monoclonal anti-phospho-cofilin (Ser[3]) (catalogue no. sc12912R), anti-cofilin (catalogue no. sc33779), anti-actin antibody (catalogue no. sc1616R), and anti-His probe (H-3) (catalogue no. sc8036) were purchased from Santa Cruz Biotechnology, Inc. For affinity purification, nickel-nitrilotriacetic acid (Ni-NTA) resin was obtained from Roche Applied Science, and GSH-Sepharose 4B was purchased from GE Healthcare Life Sciences. Tosylpheny-

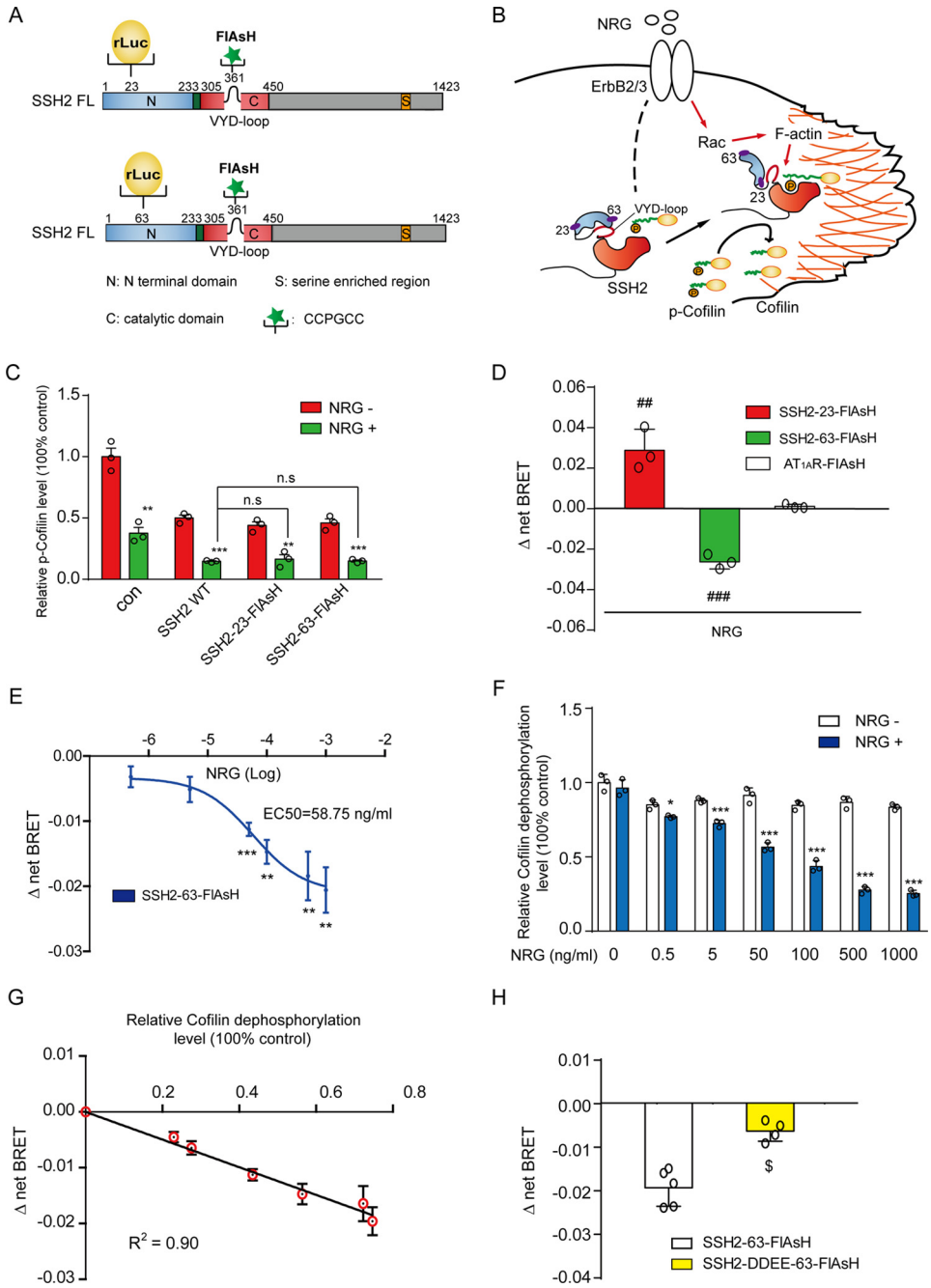

lalanyl chloromethyl ketone–treated trypsin (catalogue no. T1426) was ordered from Sigma. Monobromobimane probe was obtained from Thermo Fisher Scientific. Cell culture medium and fetal bovine serum were ordered from Hyclone GE Healthcare. Lipofectamine 2000 transfection reagent and the TC-FlAsH II In-Cell tetracysteine detection reagent were purchased from Invitrogen. NRG was ordered from Novoprotein. The coelenterazine was obtained from Promega.

Plasmid construction

Human full-length SSH1 and SSH2 were originally kind gifts from Dr. Lefkowitz (Duke University) and Dr. Zhong-Yin Zhang (Purdue University). Their *E. coli* expression constructs and derivative truncations (see Table S1 for detailed information) were subcloned into pET-15b and pGEX-6P-2, respectively, resulting in plasmid coding for N-terminally His_6-tagged or GST fusion proteins. For fluorescent probe monobromobimane (mBBr) labeling, SSH2 single cysteine mutants were constructed by introducing a cysteine residue into specified positions of SSH2 cysteine minus mutant in which all potential reactive cysteines were replaced by serines (see Fig. 5*A*). We subcloned SSH2(1–1423) into pCDNA3.1 vector with an His_6 tag at the N terminus. Then we added the rLuc into the 23- and 63-positions. The two plasmids were constructed by introducing an amino acid motif, CCPGCC, following amino acid residue 361 of SSH2 (see Fig. 6*A*). All SSH2 point mutations were obtained by PCR amplification following the standard operating procedure of the QuikChange site-directed mutagenesis kit (Stratagene) using plasmid coding for GST-tagged SSH2 as the template. The sequences of WT and mutant SSH2 were verified by DNA sequencing. Oligonucleotides used in this study are listed in Table S3.

Expression and purification of SSH2

Plasmids coding for His-tagged WT and mutant SSHs were transformed in *E. coli* BL21(DE3) cells and followed by isopropyl-1-thio-β-D-galactopyranoside (IPTG) induction as described previously (46). When absorbance at 600 nm for cell cultures grown in lysogeny broth medium was between 0.6 and 0.8, IPTG was added to a final concentration of 0.1–0.3 mM, and the culture was further induced at 23 °C for 12–16 h. The His_6-tagged proteins were purified by Ni-NTA resin as described previously (44). After a 2-h incubation of lysates with Ni-NTA–agarose a 4 °C by gentle rotation, the agarose was washed with His buffer (25 mM Tris-HCl, pH 7.5, 150 mM NaCl) 3–4 times. This washing step can get rid of most nonspecific proteins. After the wash, different concentrations were prepared of imidazole elution buffer, which contains 20, 50, 100, 200, or 300 mM imidazole. We normally concentrated protein to a final concentration between 1 and 10 mg/ml and used the centrifugal filter (Millipore) by centrifuging at 4 °C. During the concentration, the protein was changed to the HN (20 mM Hepes, pH 7.5, 100 mM NaCl, 1 mM DTT) buffer to eliminate the imidazole. SDS-PAGE was used to determine the purity of the protein. The proteins were further purified by size-exclusion chromatography. The purity of the His-SSH2 was over 95% as examined.

The procedure to purify GST-tagged protein was similar to that described previously (43). Plasmids coding for GST tag SSHs and mutations were transformed in *E. coli* BL21(DE3) cells and induced by 300 μM IPTG for 16 h at 23 °C until OD reached 0.8–1.0. The GST-tagged proteins were purified by GSH-Sepharose 4B. Bacteria were resuspended in chilled GST buffer (25 mM Tris-HCl, pH 8.0, 150 mM NaCl, 0.5% Triton X-100, 5% glycerol, 1 mM EDTA, 2 mM DTT). The cells were broken, and then the lysis was transferred into tubes to spin at 12,000 rpm for 30 min. The supernatant was removed and incubated with GSH beads for 2 h at 4 °C by gentle rotation. Beads were washed at least 3 times with GST buffer and then resuspended in GST elution buffer (10 mM reduced GSH prepared with GST buffer). Beads were spun at a lower speed, always 800 rpm, for 5 min. The supernatant was transferred into a centrifugal filter (Millipore) column to spin at 4000 rpm. The protein concentration was determined by A_{280} and Coomassie Blue staining.

Steady-state kinetics

All enzymological assays were carried out at 30 °C in 96-well plates using 3,3-dimethylglutaric acid (DMG) buffer (50 mM DMG, pH 7.0, 1 mM EDTA, 2 mM DTT; the ionic strength was

Figure 6. BRET sensors for receptor-dependent activation and conformational changes of Slingshot2. *A*, design of BRET-based Slingshot2 biosensors. Shown is a *schematic representation* of the rLuc-Slingshot2-FlAsH constructs used in this study. Two rLuc-SSH2-FlAsH were constructed by introducing rLuc in the 23 and 63 sites separately, according to biochemical results in Fig. 5. The FlAsH motif CCPGCC was incorporated at the 361 site of the VYD loop. Positions of the FlAsH-binding motif and rLuc insertion positions are *highlighted*. The sensors were termed SSH2–23-FlAsH and SSH2–63-FlAsH, respectively. *B*, schematic representation of the Slingshot activation and phospho-cofilin dephosphorylation in NRG-mediated cell motility. Activation of the ErbB2/3 by NRG leads to Rac activation and translocation of the Slingshot to the leading edge, enabling the interaction of the Slingshot with the F-actin and subsequent cofilin dephosphorylation (6, 57, 58). *C*, the function of SSH2-FlAsH biosensors in a cellular context. MCF-7 cells transfected with SSH2 WT, SSH2–23-FlAsH, and SSH2–63-FlAsH were starved for 2 h and then stimulated with 50 ng/ml NRG or control vehicle for 40 min. A *bar graph representation* and statistical quantification of the cofilin-$pSer^3$ phosphorylation level are shown. These data indicated that the SSH2-FlAsH biosensors maintain their functional integrity. *D*, intramolecular BRET of the SSH2-FlAsH biosensors in response to NRG stimulation (50 ng/ml NRG, 40 min). The BRET biosensor of the AT1R was used as a negative control (59). The SSH2–23-FlAsH, SSH2–63-FlAsH, and AT1R-FlAsH (23) were transiently transfected in MCF-7 cells, starved for 2 h, and then stimulated with 50 ng/ml NRG or control vehicle for 40 min. The Δ net BRET changes were calculated by subtraction of the BRET signal of NRG-treated cells from the control vehicle-treated cells. Whereas the NRG increased the intramolecular BRET of the SSH2–23-FlAsH biosensor, it significantly reduced the intramolecular BRET of the SSH2–63-FlAsH biosensor. *E*, concentration dependence of the NRG-induced SSH2 conformational changes reported by SSH2-FlAsH biosensors. MCF-7 cells were transfected with the plasmid SSH2–63-FlAsH. Stimulations were for 40 min using the indicated concentration. *F*, concentration dependence of the NRG induced decrease of cofilin-$pSer^3$ level. Immunoblotting was carried out by using specific antibody against $pSer^3$-cofilin, total cofilin, and His probe. Cells were transfected with SSH2–63-FlAsH. Stimulations were 40 min. Control vehicle-treated cells were used as negative controls. *G*, the relative relationship of NRG-induced p-cofilin level and FlAsH BRET. The *bar graph* represents the mean ± S.D. (*error bars*) quantified from at least three independent experiments. ##, $p < 0.01$; ###, $p < 0.005$; Slingshot WT or biosensor–transfected cells were compared with AT1R plasmid–transfected cells. *, $p < 0.05$; **, $p < 0.01$; ***, $p < 0.005$. NRG-treated cells were compared with control vehicle-treated cells. *n.s.*, no significance. *H*, the conformational change of SSH2-DDEE mutant (Ser^{21} and Ser^{25} were mutated to Asp, Ser^{32} and Ser^{36} were mutated to Glu) in response to NRG stimulation. The SSH2-DDEE-63-FlAsH construct was made by the QuikChange method. MCF-7 cells were transfected with the plasmid SSH2–63-FlAsH and SSH2-DDEE-63-FlAsH with equal amount. 100 ng/μl NRG were administrated for 40 min. Shown is a *bar graph representation* of Δ net BRET in the absence or presence of NRG stimulation. $, $p < 0.05$; DDEE mutant was compared with WT.

adjusted to 0.15 M by NaCl) as described previously (43, 46), unless otherwise specified. All reactions were initiated by the addition of appropriate amount of SSH2 into the reaction mixtures containing different substrates at various concentrations, except that, in the experiment to examine the effect of F-actin on activation of SSH2 phosphatase activity, SSH2 (0.4 μM) was preincubated with F-actin (4 μM) at room temperature for 30 min before use. For *p*NPP and OMFP, reaction was terminated by the addition of an equal volume of 1 M NaOH, and the hydrolyzed products were determined by measuring the absorbance at 405 and 477 nm, respectively. For DiFMUP and all pTyr-, pSer-, pThr-containing phosphopeptides, reactions were quenched by Biomol Green reagent, and the production of P_i was detected by monitoring the absorbance at 620 nm as described previously (47). Kinetic parameters were fitted to the Michaelis–Menten equation (Equation 1) as described previously (48). To examine the catalytic activity of SSH2 toward physiological substrate p-cofilin, SSH2 (0.4 μM) was incubated with 0.4 mM p-cofilin in a total volume of 50 μl of assay buffer (20 mM Tris-HCl, pH 7.5, 150 mM NaCl, 1 mM EDTA, and 2 mM DTT). The reaction was stopped at different time intervals, and the phosphorylation level of cofilin was examined by immunoblotting with anti-phospho-cofilin antibody. Quantification of signal intensities from three immunoblots was done using ImageJ software (National Institutes of Health). The data were analyzed by GraphPad Prism version 5 (GraphPad Software).

$$k_{cat} = [S]/(K_m + [S]) \quad \text{(Eq. 1)}$$

P_i assay of p-cofilin protein dephosphorylation by SSH2 in vitro

The dephosphorylation was performed in a reaction buffer containing 20 mM Tris-HCl, pH 7.0, 100 mM NaCl, 2 mM DTT at 37 °C. The initial p-cofilin concentration was 2 μM, and then it was diluted hole by hole in a 96-well plate with or without SSH2. The reaction was terminated by Biomol Green (Enzo Life Sciences) after that, with the end-point reading at 620 nm.

The inhibition assay

The inhibition mode for SSH2 N-terminal region was determined by examining the effects of SSH2(1–227) on SSH2 (catalytic domain)–catalyzed *p*NPP or p-cofilin protein hydrolysis in DMG buffer at 30 °C. The data were fitted to the Lineweaver–Burk equation (Equation 2) as described previously (48).

$$1/(K_m + [S])/(V_{max} \times [S]) = (K_m/V_{max}) \times (1/[S]) + 1/V_{max} \quad \text{(Eq. 2)}$$

pH profile assay

Effects of pH on SSH2-catalyzed hydrolysis of *p*NPP were performed in the following buffers: 50 mM succinate, pH 5.0–6.5; 50 mM DMG, pH 6.6–7.5; 50 mM Tris, pH 7.5–8.5. All of the above-mentioned reaction buffers contained 1 mM EDTA, 2 mM DTT, and the ionic strengths were adjusted to 0.15 M using NaCl. The k_{cat} and k_{cat}/K_m values for different SSH2 truncations were measured in various buffers using *p*NPP as the substrate. Then the data were fitted to the Michaelis–Menten equation (Equation 1) as described previously. After that, k_{cat}/K_m *versus* pH profile values and the k_{cat} *versus* pH profile values were fitted to Equations 3 and 4 as described previously (46, 49),

$$k_{cat}/K_m = (k_{cat}/K_m)^{lim}/(1 + (H/K_{s2}))/(1 + (H/K_{E1}) + (K_{E2}/H)) \quad \text{(Eq. 3)}$$

$$k_{cat} = (k_{cat})^{lim}/1 + (H/K_1^{app}) + (K_2^{app}/H) \quad \text{(Eq. 4)}$$

where H is the proton concentration.

Leaving-group dependence

The assays were conducted in 50 mM DMG buffer (pH 7.0, 1 mM EDTA, 2 mM DTT with a 0.15 M ionic strength) at 30 °C. Small molecular substrates with different pK_a (*p*NPP, 7.14; MUP, 7.8; 2-naphthyl phosphate sodium salt, 9.38; *O*-phospho-L-tyrosine, 10.04) were used as substrates in this assay (50, 51). The k_{cat} and k_{cat}/K_m data were fitted to the Michaelis–Menten equation (Equation 1) as described previously (46, 52). Log(k_{cat}) and log(k_{cat}/K_m) values were plotted against the leaving-group pK_a of the substrates to derive the leaving-group dependence curve, and the β_{1g} values were acquired. All data were analyzed by GraphPad Prism version 5 (GraphPad Software).

Preparation of F-actin

Skeletal G-actin was extracted from rabbit hind leg muscle and stored in G buffer (5 mM Tris-HCl, pH 8.0, 0.2 mM ATP, 1 mM DTT, 0.1 mM $CaCl_2$, and 1 mM NaN_3) at a concentration of 10 μM as described previously (53). To convert G-actin to F-actin, $MgCl_2$ was added to G-actin solution to a final concentration of 2 mM, and KCl was added to a final concentration of 0.8 M. The reaction mixture was further incubated at 4 °C for 1 h with stirring, and polymerized F-actin was collected by centrifugation at 100,000 × *g* for 1 h. F-actin pellets at the bottom of tubes were resuspended with F buffer (15 mM HEPES, pH 7.5, 50 mM KCl, 1 mM $MgCl_2$, 0.1 mM EGTA, 0.005% NaN_3).

Limited trypsin proteolysis

The limited trypsin digestion reactions were performed as described previously (54), with minor modifications. A total of 500 μg of SSH2(1–490) (or SSH2(1–455)) at 2 μM, premixed with or without 4 μM F-actin, or F-actin alone was incubated with tosylphenylalanyl chloromethyl ketone–treated trypsin at a trypsin/SSH2 mass ratio of 1:1000 in 20 mM Tris-HCl, pH 7.5, 150 mM NaCl. The reaction mixtures were maintained at 37 °C. Aliquots were collected at 0, 15, and 30 min and analyzed by SDS-PAGE to determine the effects of F-actin on the digestion pattern. For precise trypsin cleavage site analysis, samples were further subjected to protein sequencing using Edman degradation as described previously (28). The N-terminal protein sequencing was performed by the Beijing Agricultural Biology Monitoring Center.

Labeling of SSH2 with mBBr

Labeling of the SSH2 with mBBr was carried out using a protocol described previously (31, 47). A noncysteine-GST tag was achieved by mutation of all four cysteines in GST to Ser.

The resulted GST-noncysteine construct showed normal GST bead–binding activity. Briefly, GST-noncysteine-tagged single-cysteine SSH2 mutation proteins were buffer-exchanged three times using labeling buffer containing 10 mM MES, pH 6.5, 150 mM NaCl. The mutants were ultracentrifuged to a final concentration of 50 μM and incubated with a 10-fold molar excess of mBBr (stock in 1% DMSO) at room temperature for 3 h with gentle rotation. The reaction mixtures were then centrifuged at 12,000 rpm for 30 min, and the supernatants were further incubated with GSH resin for 1 h. SSH2 bound to GSH resin was washed extensively with washing buffer (10 mM Hepes, pH 7.4, 250 mM NaCl) and eluted by 10 mM GSH. The mBBr-labeled SSH2 was further purified by size-exclusion chromatography using a buffer containing 10 mM Hepes, pH 7.4, 150 mM NaCl and concentrated to 20 μM. The calculation of the labeling efficiency was performed as described previously (55).

Fluorescence spectroscopy

For the fluorescence spectroscopy assay, reactions were performed in a final volume of 100 μl in reaction buffer (10 mM Hepes, pH 7.4, 150 mM NaCl) containing mBBr-labeled SSH2 mutants (2 μM) with or without F-actin (4 μM). The bimane fluorophore was excited at 390 nm, and emission was collected between 410 and 600 nm (2-nm step size, 0.5-s integration per point) as described previously (47).

Cell culture and transfection

MCF-7 cells were maintained in high-glucose minimum essential medium supplemented with 10% fetal bovine serum and 1% antibiotic/antimycotic solution. Transfections were performed using Lipofectamine 2000. The cells' confluence was ~90–95% before transfection, and the signaling assays were performed with cell confluence at ~75%.

Intramolecular FlAsH BRET assay

MCF-7 cells were seeded in 6-well plates after transfection with AT1R-FlAsH (as a control), SSH2 WT, SSH2–23-FlAsH, and SSH2–63-FlAsH with rLuc inserted in a specific N-terminal site. Before the BRET assay, MCF-7 cells were starved with serum for 1 h. Then cells were digested, centrifuged, and resuspended in 500 μl of BRET buffer (25 mM Hepes, 1 mM $CaCl_2$, 140 mM NaCl, 2.7 mM KCl, 0.9 mM $MgCl_2$, 0.37 mM NaH_2PO_4, 5.5 mM D-glucose, 12 mM $NaHCO_3$). The TC-FlAsH reagent was added at a final concentration of 2.5 μM and incubated at 37 °C for ~1 h. Subsequently, cells were washed with BRET buffer and then distributed into white-wall clear-bottom 96-well plates, with ~100,000 cells/well. The cells were treated with 50 ng/ml NRG at 37 °C for 15–20 min, and then coelenterazinc was added at a final concentration of 5 μM, followed immediately by checking of the luciferase (440–480 nm) and TC-FlAsH (525–585 nm) emissions. The BRET ratio (emission enhanced yellow fluorescent protein/emission rLuc) calculated using a Berthold Technologies Tristar 3 LB 941 spectrofluorimeter. The procedure was modified from those described previously (32, 56).

In vitro pulldown assay

SSH2 WT, SSH2–23-FlAsH, and SSH2–63-FlAsH with a His tag at their N termini were transfected into three 150-mm plates of MCF-7 cells for purification. Lysates were incubated with Ni-NTA–agarose at 4 °C for about 2 h with gentle rotation. After centrifugation, pallets were washed and eluted with gradient imidazole. The fraction containing the Slingshot was analyzed by immunoblotting with His-antibody and collected accordingly. The purity of these proteins was examined by Western blotting. The enzyme activity was assayed using the substrate *p*NPP or phospho-cofilin protein (see Fig. 6 (*D* and *E*) and Fig. S11).

Statistics

All of the Western blots were performed independently at least three times, and the data are presented as the mean ± S.D. All kinetic data are presented as the mean ± S.E. of more than three independent experiments. Statistical comparisons were analyzed using analysis of variance with GraphPad Prism version 5 or GraphPad Prism version 7.

Author contributions—J. S. and J. W. initiated the research. J. S., X. Y., J. W., and P. X. designed all of the experiments. J. S., J. W., and X. Y. supervised the overall project design and execution. D. Y., P. X., Q. L., X. Y., and J. S. participated in data analysis and interpretation. D. Y., Q. L., X. F., C. P., D. L., S. W., H. L., and W. X. performed cell biology and molecular biology experiments. D. Y., P. X., D. H., H. F., Y. S., and Z. X performed biochemistry experiments. C. W. performed molecular cloning experiments. A. L., X. Y., and J. S. provided insightful ideas and experimental designs. J. W., X. Y., and J. S. wrote the manuscript. All of the authors have seen and commented on the manuscript.

References

1. Ng, J., and Luo, L. (2004) Rho GTPases regulate axon growth through convergent and divergent signaling pathways. *Neuron* **44,** 779–793 CrossRef Medline
2. Wen, Z., Han, L., Bamburg, J. R., Shim, S., Ming, G. L., and Zheng, J. Q. (2007) BMP gradients steer nerve growth cones by a balancing act of LIM kinase and Slingshot phosphatase on ADF/cofilin. *J. Cell Biol.* **178,** 107–119 CrossRef Medline
3. Endo, M., Ohashi, K., Sasaki, Y., Goshima, Y., Niwa, R., Uemura, T., and Mizuno, K. (2003) Control of growth cone motility and morphology by LIM kinase and Slingshot via phosphorylation and dephosphorylation of cofilin. *J. Neurosci.* **23,** 2527–2537 CrossRef Medline
4. Xu, X., Gera, N., Li, H., Yun, M., Zhang, L., Wang, Y., Wang, Q. J., and Jin, T. (2015) GPCR-mediated PLC$\beta\gamma$/PKCβ/PKD signaling pathway regulates the cofilin phosphatase slingshot 2 in neutrophil chemotaxis. *Mol. Biol. Cell* **26,** 874–886 CrossRef Medline
5. Bielig, H., Lautz, K., Braun, P. R., Menning, M., Machuy, N., Brügmann, C., Barisic, S., Eisler, S. A., Andree, M., Zurek, B., Kashkar, H., Sansonetti, P. J., Hausser, A., Meyer, T. F., and Kufer, T. A. (2014) The cofilin phosphatase slingshot homolog 1 (SSH1) links NOD1 signaling to actin remodeling. *PLoS Pathog.* **10,** e1004351 CrossRef Medline
6. Mizuno, K. (2013) Signaling mechanisms and functional roles of cofilin phosphorylation and dephosphorylation. *Cell. Signal.* **25,** 457–469 CrossRef Medline
7. Kaji, N., Ohashi, K., Shuin, M., Niwa, R., Uemura, T., and Mizuno, K. (2003) Cell cycle-associated changes in Slingshot phosphatase activity and roles in cytokinesis in animal cells. *J. Biol. Chem.* **278,** 33450–33455 CrossRef Medline

8. Lu, X., Boora, U., Seabra, L., Rabai, E. M., Fenton, J., Reiman, A., Nagy, Z., and Maher, E. R. (2014) Knockdown of Slingshot 2 (SSH2) serine phosphatase induces Caspase3 activation in human carcinoma cell lines with the loss of the Birt-Hogg-Dube tumour suppressor gene (FLCN). *Oncogene* **33,** 956–965 CrossRef Medline
9. Horita, Y., Ohashi, K., Mukai, M., Inoue, M., and Mizuno, K. (2008) Suppression of the invasive capacity of rat ascites hepatoma cells by knockdown of Slingshot or LIM kinase. *J. Biol. Chem.* **283,** 6013–6021 CrossRef Medline
10. Dai, S., Sarmiere, P. D., Wiggan, O., Bamburg, J. R., and Zhou, D. (2004) Efficient *Salmonella* entry requires activity cycles of host ADF and cofilin. *Cell. Microbiol.* **6,** 459–471 CrossRef Medline
11. Woo, J. A., Zhao, X., Khan, H., Penn, C., Wang, X., Joly-Amado, A., Weeber, E., Morgan, D., and Kang, D. E. (2015) Slingshot-cofilin activation mediates mitochondrial and synaptic dysfunction via Aβ ligation to β1-integrin conformers. *Cell Death Differ.* **22,** 1069–1070 CrossRef Medline
12. Yamashiro, Y., Papke, C. L., Kim, J., Ringuette, L. J., Zhang, Q. J., Liu, Z. P., Mirzaei, H., Wagenseil, J. E., Davis, E. C., and Yanagisawa, H. (2015) Abnormal mechanosensing and cofilin activation promote the progression of ascending aortic aneurysms in mice. *Sci. Signal.* **8,** ra105 CrossRef Medline
13. Torres, R. A., Drake, D. A., Solodushko, V., Jadhav, R., Smith, E., Rocic, P., and Weber, D. S. (2011) Slingshot isoform-specific regulation of cofilin-mediated vascular smooth muscle cell migration and neointima formation. *Arterioscler. Thromb Vasc. Biol.* **31,** 2424–2431 CrossRef Medline
14. Park, H., Park, S. Y., and Ryu, S. E. (2013) Homology modeling and virtual screening approaches to identify potent inhibitors of slingshot phosphatase 1. *J. Mol. Graph. Model.* **39,** 65–70 CrossRef Medline
15. Lee, S. Y., Kim, W., Lee, Y. G., Kang, H. J., Lee, S. H., Park, S. Y., Min, J. K., Lee, S. R., and Chung, S. J. (2017) Identification of sennoside A as a novel inhibitor of the slingshot (SSH) family proteins related to cancer metastasis. *Pharmacol. Res.* **119,** 422–430 CrossRef Medline
16. Kurita, S., Watanabe, Y., Gunji, E., Ohashi, K., and Mizuno, K. (2008) Molecular dissection of the mechanisms of substrate recognition and F-actin-mediated activation of cofilin-phosphatase Slingshot-1. *J. Biol. Chem.* **283,** 32542–32552 CrossRef Medline
17. Maheswaranathan, M., Gole, H. K., Fernandez, I., Lassègue, B., Griendling, K. K., and San Martín, A. (2011) Platelet-derived growth factor (PDGF) regulates Slingshot phosphatase activity via Nox1-dependent auto-dephosphorylation of serine 834 in vascular smooth muscle cells. *J. Biol. Chem.* **286,** 35430–35437 CrossRef Medline
18. Eiseler, T., Döppler, H., Yan, I. K., Kitatani, K., Mizuno, K., and Storz, P. (2009) Protein kinase D1 regulates cofilin-mediated F-actin reorganization and cell motility through slingshot. *Nat. Cell Biol.* **11,** 545–556 CrossRef Medline
19. Tang, W., Zhang, Y., Xu, W., Harden, T. K., Sondek, J., Sun, L., Li, L., and Wu, D. (2011) A PLCβ/PI3Kγ-GSK3 signaling pathway regulates cofilin phosphatase slingshot2 and neutrophil polarization and chemotaxis. *Dev. Cell* **21,** 1038–1050 CrossRef Medline
20. Gilmartin, A. G., Faitg, T. H., Richter, M., Groy, A., Seefeld, M. A., Darcy, M. G., Peng, X., Federowicz, K., Yang, J., Zhang, S. Y., Minthorn, E., Jaworski, J. P., Schaber, M., Martens, S., McNulty, D. E., *et al.* (2014) Allosteric Wip1 phosphatase inhibition through flap-subdomain interaction. *Nat. Chem. Biol.* **10,** 181–187 CrossRef Medline
21. Chen, Y. N., LaMarche, M. J., Chan, H. M., Fekkes, P., Garcia-Fortanet, J., Acker, M. G., Antonakos, B., Chen, C. H., Chen, Z., Cooke, V. G., Dobson, J. R., Deng, Z., Fei, F., Firestone, B., Fodor, M., *et al.* (2016) Allosteric inhibition of SHP2 phosphatase inhibits cancers driven by receptor tyrosine kinases. *Nature* **535,** 148–152 CrossRef Medline
22. Almer, H., and Stromberg, R. (1996) Base catalysis and leaving group dependence in intramolecular alcoholysis of uridine 3′-(aryl phosphorothioate)s. *J. Am. Chem. Soc.* **118,** 7921–7928 CrossRef
23. Liu, C. H., Gong, Z., Liang, Z. L., Liu, Z. X., Yang, F., Sun, Y. J., Ma, M. L., Wang, Y. J., Ji, C. R., Wang, Y. H., Wang, M. J., Cui, F. A., Lin, A., Zheng, W. S., He, D. F., *et al.* (2017) Arrestin-biased AT1R agonism induces acute catecholamine secretion through TRPC3 coupling. *Nat. Commun.* **8,** 14335 CrossRef Medline
24. Takahashi, K., Okabe, H., Kanno, S. I., Nagai, T., and Mizuno, K. (2017) A pleckstrin homology-like domain is critical for F-actin binding and cofilin-phosphatase activity of Slingshot-1. *Biochem. Biophys. Res. Commun.* **482,** 686–692 CrossRef Medline
25. Liu, X., Zhang, C. S., Lu, C., Lin, S. C., Wu, J. W., and Wang, Z. X. (2016) A conserved motif in JNK/p38-specific MAPK phosphatases as a determinant for JNK1 recognition and inactivation. *Nat. Commun.* **7,** 10879 CrossRef Medline
26. Anyatonwu, G., Khan, M. T., Schug, Z. T., da Fonseca, P. C., Morris, E. P., and Joseph, S. K. (2010) Calcium-dependent conformational changes in inositol trisphosphate receptors. *J. Biol. Chem.* **285,** 25085–25093 CrossRef Medline
27. Mayer, C., Neubert, M., and Grummt, I. (2008) The structure of NoRC-associated RNA is crucial for targeting the chromatin remodelling complex NoRC to the nucleolus. *EMBO Rep.* **9,** 774–780 CrossRef Medline
28. Xiao, K., Shenoy, S. K., Nobles, K., and Lefkowitz, R. J. (2004) Activation-dependent conformational changes in {beta}-arrestin 2. *J. Biol. Chem.* **279,** 55744–55753 CrossRef Medline
29. Jung, S. K., Jeong, D. G., Yoon, T. S., Kim, J. H., Ryu, S. E., and Kim, S. J. (2007) Crystal structure of human slingshot phosphatase 2. *Proteins* **68,** 408–412 CrossRef Medline
30. Dawaliby, R., Trubbia, C., Delporte, C., Masureel, M., Van Antwerpen, P., Kobilka, B. K., and Govaerts, C. (2016) Allosteric regulation of G protein-coupled receptor activity by phospholipids. *Nat. Chem. Biol.* **12,** 35–39 CrossRef Medline
31. Kim, Y. J., Hofmann, K. P., Ernst, O. P., Scheerer, P., Choe, H. W., and Sommer, M. E. (2013) Crystal structure of pre-activated arrestin p44. *Nature* **497,** 142–146 CrossRef Medline
32. Nuber, S., Zabel, U., Lorenz, K., Nuber, A., Milligan, G., Tobin, A. B., Lohse, M. J., and Hoffmann, C. (2016) β-Arrestin biosensors reveal a rapid, receptor-dependent activation/deactivation cycle. *Nature* **531,** 661–664 CrossRef Medline
33. Hubbard, S. R. (2004) Juxtamembrane autoinhibition in receptor tyrosine kinases. *Nat. Rev. Mol. Cell Biol.* **5,** 464–471 CrossRef Medline
34. Wang, Q., Vogan, E. M., Nocka, L. M., Rosen, C. E., Zorn, J. A., Harrison, S. C., and Kuriyan, J. (2015) Autoinhibition of Bruton's tyrosine kinase (Btk) and activation by soluble inositol hexakisphosphate. *eLife* **4,** 0.7554/eLife.06074 CrossRef Medline
35. Endres, N. F., Engel, K., Das, R., Kovacs, E., and Kuriyan, J. (2011) Regulation of the catalytic activity of the EGF receptor. *Curr. Opin. Struct. Biol.* **21,** 777–784 CrossRef Medline
36. Li, S. J., Wang, J., Ma, L., Lu, C., Wang, J., Wu, J. W., and Wang, Z. X. (2016) Cooperative autoinhibition and multi-level activation mechanisms of calcineurin. *Cell Res.* **26,** 336–349 CrossRef Medline
37. Matozaki, T., Murata, Y., Saito, Y., Okazawa, H., and Ohnishi, H. (2009) Protein tyrosine phosphatase SHP-2: a proto-oncogene product that promotes Ras activation. *Cancer science* **100,** 1786–1793 CrossRef Medline
38. Ostman, A., Hellberg, C., and Böhmer, F. D. (2006) Protein-tyrosine phosphatases and cancer. *Nat. Rev. Cancer* **6,** 307–320 CrossRef Medline
39. Lechleider, R. J., Sugimoto, S., Bennett, A. M., Kashishian, A. S., Cooper, J. A., Shoelson, S. E., Walsh, C. T., and Neel, B. G. (1993) Activation of the SH2-containing phosphotyrosine phosphatase SH-PTP2 by its binding site, phosphotyrosine 1009, on the human platelet-derived growth factor receptor. *J. Biol. Chem.* **268,** 21478–21481 Medline
40. Hof, P., Pluskey, S., Dhe-Paganon, S., Eck, M. J., and Shoelson, S. E. (1998) Crystal structure of the tyrosine phosphatase SHP-2. *Cell* **92,** 441–450 CrossRef Medline
41. Zhang, K., Zhao, H., Ji, Z., Zhang, C., Zhou, P., Wang, L., Chen, Q., Wang, J., Zhang, P., Chen, Z., Zhu, H. H., and Gao, W. Q. (2016) Shp2 promotes metastasis of prostate cancer by attenuating the PAR3/PAR6/aPKC polarity protein complex and enhancing epithelial-to-mesenchymal transition. *Oncogene* **35,** 1271–1282 CrossRef Medline
42. Li, R., Gong, Z., Pan, C., Xie, D. D., Tang, J. Y., Cui, M., Xu, Y. F., Yao, W., Pang, Q., Xu, Z. G., Li, M. Y., Yu, X., and Sun, J. P. (2013) Metal-dependent protein phosphatase 1A functions as an extracellular signal-regulated kinase phosphatase. *FEBS J.* **280,** 2700–2711 CrossRef Medline
43. Wang, H. M., Xu, Y. F., Ning, S. L., Yang, D. X., Li, Y., Du, Y. J., Yang, F., Zhang, Y., Liang, N., Yao, W., Zhang, L. L., Gu, L. C., Gao, C. J., Pang, Q.,

Chen, Y. X., *et al.* (2014) The catalytic region and PEST domain of PTPN18 distinctly regulate the HER2 phosphorylation and ubiquitination barcodes. *Cell Res.* **24,** 1067–1090 CrossRef Medline

44. Li, H., Yang, F., Liu, C., Xiao, P., Xu, Y., Liang, Z., Liu, C., Wang, H., Wang, W., Zheng, W., Zhang, W., Ma, X., He, D., Song, X., Cui, F., *et al.* (2016) Crystal structure and substrate specificity of PTPN12. *Cell Rep.* **15,** 1345–1358 CrossRef Medline
45. Yang, F., Yu, X., Liu, C., Qu, C. X., Gong, Z., Liu, H. D., Li, F. H., Wang, H. M., He, D. F., Yi, F., Song, C., Tian, C. L., Xiao, K. H., Wang, J. Y., and Sun, J. P. (2015) Phospho-selective mechanisms of arrestin conformations and functions revealed by unnatural amino acid incorporation and (19)F-NMR. *Nat. Commun.* **6,** 8202 CrossRef Medline
46. Xiao, P., Wang, X., Wang, H. M., Fu, X. L., Cui, F. A., Yu, X., Wen, S. S., Bi, W. X., and Sun, J. P. (2014) The second-sphere residue T263 is important for the function and catalytic activity of PTP1B via interaction with the WPD-loop. *Int. J. Biochem. Cell Biol.* **57,** 84–95 CrossRef Medline
47. Yao, X., Parnot, C., Deupi, X., Ratnala, V. R., Swaminath, G., Farrens, D., and Kobilka, B. (2006) Coupling ligand structure to specific conformational switches in the β2-adrenoceptor. *Nat. Chem. Biol.* **2,** 417–422 CrossRef Medline
48. Pan, C., Liu, H. D., Gong, Z., Yu, X., Hou, X. B., Xie, D. D., Zhu, X. B., Li, H. W., Tang, J. Y., Xu, Y. F., Yu, J. Q., Zhang, L. Y., Fang, H., Xiao, K. H., Chen, Y. G., *et al.* (2013) Cadmium is a potent inhibitor of PPM phosphatases and targets the M1 binding site. *Sci. Rep.* **3,** 2333 CrossRef Medline
49. Wu, L., and Zhang, Z. Y. (1996) Probing the function of Asp128 in the lower molecular weight protein-tyrosine phosphatase-catalyzed reaction: a pre-steady-state and steady-state kinetic investigation. *Biochemistry* **35,** 5426–5434 CrossRef Medline
50. Zhang, Z. Y., and VanEtten, R. L. (1991) Pre-steady-state and steady-state kinetic analysis of the low molecular weight phosphotyrosyl protein phosphatase from bovine heart. *J. Biol. Chem.* **266,** 1516–1525 Medline
51. Wang, W. Q., Bembenek, J., Gee, K. R., Yu, H., Charbonneau, H., and Zhang, Z. Y. (2004) Kinetic and mechanistic studies of a cell cycle protein phosphatase Cdc14. *J. Biol. Chem.* **279,** 30459–30468 CrossRef Medline
52. Pedersen, A. K., Guo, X. L., Møller, K. B., Peters, G. H., Andersen, H. S., Kastrup, J. S., Mortensen, S. B., Iversen, L. F., Zhang, Z. Y., and Møller, N. P. (2004) Residue 182 influences the second step of protein-tyrosine phosphatase-mediated catalysis. *Biochem. J.* **378,** 421–433 CrossRef Medline
53. Selden, L. A., Kinosian, H. J., Estes, J. E., and Gershman, L. C. (2000) Cross-linked dimers with nucleating activity in actin prepared from muscle acetone powder. *Biochemistry* **39,** 64–74 CrossRef Medline
54. Nobles, K. N., Guan, Z., Xiao, K., Oas, T. G., and Lefkowitz, R. J. (2007) The active conformation of β-arrestin1: direct evidence for the phosphate sensor in the N-domain and conformational differences in the active states of β-arrestins1 and -2. *J. Biol. Chem.* **282,** 21370–21381 CrossRef Medline
55. Sommer, M. E., Smith, W. C., and Farrens, D. L. (2005) Dynamics of arrestin-rhodopsin interactions: arrestin and retinal release are directly linked events. *J. Biol. Chem.* **280,** 6861–6871 CrossRef Medline
56. Lee, M. H., Appleton, K. M., Strungs, E. G., Kwon, J. Y., Morinelli, T. A., Peterson, Y. K., Laporte, S. A., and Luttrell, L. M. (2016) The conformational signature of β-arrestin2 predicts its trafficking and signalling functions. *Nature* **531,** 665–668 CrossRef Medline
57. Döppler, H., Bastea, L. I., Eiseler, T., and Storz, P. (2013) Neuregulin mediates F-actin-driven cell migration through inhibition of protein kinase D1 via Rac1 protein. *J. Biol. Chem.* **288,** 455–465 CrossRef Medline
58. Sparrow, N., Manetti, M. E., Bott, M., Fabianac, T., Petrilli, A., Bates, M. L., Bunge, M. B., Lambert, S., and Fernandez-Valle, C. (2012) The actin-severing protein cofilin is downstream of neuregulin signaling and is essential for Schwann cell myelination. *J. Neurosci.* **32,** 5284–5297 CrossRef Medline
59. Li, T., Yu, B., Liu, Z., Li, J., Ma, M., Wang, Y., Zhu, M., Yin, H., Wang, X., Fu, Y., Yu, F., Wang, X., Fang, X., Sun, J., and Kong, W. (2018) Homocysteine directly interacts and activates the angiotensin II type I receptor to aggravate vascular injury. *Nat. Commun.* **9,** 11 CrossRef Medline